Article:

Stefanini, L., Ansari, D., Walkley, B. orcid.org/0000-0003-1069-1362 et al. (1 more author) (2024) Characterisation of calcined waste clays from kaolinite extraction in alkali-activated GGBFS blends. Materials Today Communications, 38. 107777. ISSN: 2352-4928

https://doi.org/10.1016/j.mtcomm.2023.107777

Materials Today Communications 38 (2024) 107777

Contents lists available at ScienceDirect

Materials Today Communications

journal homepage: www.elsevier.com/locate/mtcomm

Characterisation of calcined waste clays from kaolinite extraction in alkali-activated GGBFS blends

Laura Stefanini [a,b,*], Deeba Ansari [c], Brant Walkley [d], John L. Provis [a,e]

[a] Department of Materials Science & Engineering, University of Sheffield, Sir Robert Hadfield Building, Mappin Street, Sheffield S1 3JD, United Kingdom
[b] VTT, Technical Research Centre of Finland Ltd., Espoo, Finland
[c] Imerys, United Kingdom
[d] Department of Chemical & Biological Engineering, University of Sheffield, Sir Robert Hadfield Building, Mappin Street, Sheffield S1 3JD, United Kingdom
[e] Paul Scherrer Institut, Forschungsstrasse 111, 5232 Villigen, Switzerland

ARTICLE INFO

Keywords:
Calcined clays
Waste clays
Valorisation
Alkali-activation
Geopolymers
Ground, granulated blast furnace slag (GGBFS)
Solid state nuclear magnetic resonance (NMR) spectroscopy

ABSTRACT

Metakaolin is a well-studied supplementary cementitious material (SCM) and precursor in alkali-activation. The utilisation of limited kaolinite content clays generated from large-scale industrial activity, denoted as waste clays, in alkali-activation is still largely unexplored. This paper investigates the use of five samples of calcined waste clays from different locations in a kaolinite extraction site as precursors in alkali-activated cements (AACs). Calcined waste clay precursors are blended with ground granulated blast furnace slag (GGBFS) and activated with sodium silicate. The physical and chemical properties of the calcined waste clays are characterised. Both Chapelle and R3 tests for pozzolanic reactivity are examined based on calcined waste clay properties. The R3 test data obtained for sieved particle fractions < 63 µm show marked improvement in the case of C4, elucidating potential calcined waste clay behaviour with prior processing in alkali activated systems. Clay particle size distribution and morphology are identified as key factors to be considered for initial calcination and in mix designs, strongly affecting both the fresh properties and workability of blended pastes. Good workability is highlighted as being crucial for achieving well-behaving calcined waste clay blended binders with resulting dense microstructures and high strength values, comparable with other reported GGBFS systems. Quartz, muscovite, and alkali-feldspar present in the calcined waste clays remain stable throughout alkali-activation. Reaction of the amorphous phase fraction present in the calcined waste clays results in the formation of additional cross-linked gel. A replacement level of up to 20 wt% calcined waste clay is found to exhibit similar compressive strengths to pure GGBFS binders, whilst achieving lower porosity within the bulk. This study provides a methodology for characterising the behaviour of calcined waste clays in alkali-activated systems and a proof of concept in the formulation of novel binders that incorporate waste clays.

1. Introduction

Clay minerals are considered to be abundant, predominating in soils and sedimentary rocks found throughout the earth's crust. Clays are easily sourced from various locations globally and are generally not considered to be a limited resource. The quality and suitability of clays for use as a primary resource for given applications is, however, highly dependent on the specific mineral composition, particle morphology, and particle size [1]. Careful selection and testing of clay sources is necessary to ensure desired behaviour as a raw resource for any given process.

Calcined clays are extensively used as supplementary cementitious materials (SCMs) in concrete owing to their pozzolanic properties [2], and can be also used as a primary raw material in alkali-activation [3–5]. Kaolinite is one of the most common aluminosilicate mineral clays. Metakaolin, the anhydrous calcined form of kaolinite, is the most widely investigated type of calcined clay [6,7], due to the availability of sources with consistent elemental compositions without associated minerals, and high pozzolanic reactivity. Alkali-activation technology can potentially accommodate residues from the primary extraction of kaolinite deposits, and metakaolin sources that do not satisfy purity requirements for use as conventional SCMs, providing pathways to

---

* Corresponding author at: Department of Materials Science & Engineering, University of Sheffield, Sir Robert Hadfield Building, Mappin Street, Sheffield S1 3JD, United Kingdom.

E-mail address: laura.stefanini@vtt.fi (L. Stefanini).

https://doi.org/10.1016/j.mtcomm.2023.107777
Received 8 June 2023; Received in revised form 23 November 2023; Accepted 1 December 2023

valorise clays that are currently considered to be waste materials [8].

Literature on metakaolin based alkali-activated cements (AACs) has highlighted technical issues ranging from poor workability [9] to high water demand [10,11]. These problems are attributed to the inherent platelet-like morphology of kaolinite giving rise to high particle surface area and strong electrostatic interactions during mixing. Increasing water content to overcome these effects can lead to substantial drying shrinkage and cracking [12,13]. Changes in mix design, aimed at minimising capillary porosity, can help reducing shrinkage [14].

Blends incorporating high calcium precursors have shown promise in enhancing microstructures, forming both C-A-S-H and N-A-S-H phases [15]. The coexistence of both gel types has been corroborated through SEM–EDS and solid-state nuclear magnetic resonance (NMR) analyses in metakaolin-slag systems [16,17]. It is suggested that the coexistence of these gel types may arise from differing kinetics of dissolution and precipitation between metakaolin and slag components, without a clear dominance of one precursor [16]. This coexistence confers several benefits, including improved mechanical properties, enhanced durability, increased pore refinement and density [15,16,18]. Although the addition of calcium or slags to metakaolin has proven beneficial for performance in comparison to metakaolin-only alkali-activated materials [19–21], some studies suggest that incorporating metakaolin into a slag-based binder may require an increased concentration of activator to reach similar compressive strength to a slag-only binder, [15,18,22,23] whilst still achieving higher flexural strength [15].

Determining the optimum composition and balance between replacement level, activator dosage, and modulus of the sodium silicate activator solution proves challenging, as various studies yield differing results. Certain studies report a maximum compressive strength with 30 wt% metakaolin [24], whilst others propose 40 wt% [21], or even 50 wt % [22,25], however, some authors observe a reduction in strength with metakaolin inclusions [18]. Blends with 15 wt% metakaolin have been developed for early strength development, particularly for repair applications [26]. The controversy surrounding the identification of optimal mix design properties has led many researchers to focus on mathematical approaches for formulation optimisation. These efforts prioritise factors such as replacement level, activator dosage, and modulus of the activator aiming to optimise durability performance, mechanical properties, workability, and efflorescence. Based on this approach, favourable properties for 25 wt% metakaolin replacement activated with a modulus 1.5 sodium silicate [27] and 50 wt% metakaolin with a modulus of 1.6–1.8 [25] have been reported.

Several studies have investigated the impact of metakaolin addition on autogenous and drying shrinkage in alkali-activated slag systems. It has been observed that incorporating 20 wt% metakaolin can reduce shrinkage by 50% whilst causing only a minor reduction in the elastic modulus [28]. In cases of higher activator concentration and modulus, metakaolin additions can lead to an increase in the magnitude of autogenous and drying shrinkage in alkali-activated slag [22,24]. Consequently, finding the right balance between mix design parameters is crucial to achieving desirable material properties, especially when utilising calcined clays with low metakaolin content.

The utilisation of calcined waste clays sourced from the extraction of kaolinite, in mixed blends with a well-studied Ca-rich precursor like GGBFS is investigated. The inclusion of calcined waste clays as a possible replacement for GGBFS may provide a pathway to achieve tailored systems with coexisting C-A-S-H and N-A-S-H phases.

This study aims at the utilisation and valorisation of waste clays from industrial activity in alkali-activation for the partial replacement of GGBFS. In the first part of this study, the incorporation of 30 wt% calcined waste clays as a replacement for GGBFS in AACs activated with sodium silicate is investigated. Isothermal calorimetry, setting time, and mini-slump tests are performed to understand the fresh-state and early hydration properties. The microstructural development of the resulting alkali-activated binders is characterised using X-ray diffraction (XRD) and scanning electron microscopy (SEM). The second part of this study presents a proof of concept demonstrating that a blended binder based on 20 wt% of a selected calcined waste clay blended with 80 wt% GGBFS can reach and surpass the properties of a binder formed solely from GGBFS. The systems are characterised by isothermal calorimetry, setting times, mini slump tests, XRD, SEM, Fourier-transform infra-red (FTIR) spectroscopy, solid state NMR, and mercury intrusion porosimetry (MIP) techniques. The compressive strength is evaluated for all AACs.

2. Materials and methods

2.1. Calcined waste clays characterisation

Blends of GGBFS and calcined waste clays were used as precursors for alkali-activation. The GGBFS used was provided by ECOCEM and the calcined waste clays were sourced by Imerys UK, as a waste of kaolinite extraction from a primary kaolin deposit located in Cornwall, UK. Clays were previously calcined in a muffle furnace during 1 h at either 750 or 800 °C as indicated in Table 1. The densities of precursors, measured using a Micromeritics AccuPyc II 1340 pycnometer, and the particle size distribution, measured using a Malvern Mastersizer 3000, for all precursor materials are shown in Table 1 and Fig. 1. Both C1 and C2 exhibit multi-modal particle size distributions. C3 and C5 show similar unimodal distributions, whilst C4 has the largest average (d_{50}) particle size. The chemical oxide compositions of the calcined waste clays obtained by X-ray fluorescence are shown in Table 2. C1, C2, and C3 share a similar composition with a SiO_2/Al_2O_3 ratio of between 1.2–1.3, whereas C5 exhibits a SiO_2/Al_2O_3 ratio of $\sim$ 1.8, and that of C4 exceeds 2.8.

The XRD patterns of the precursors are presented in Fig. 2. GGBFS is amorphous with a characteristic broad peak between 25° and 35° 2θ.

The main phases identified across all calcined waste clays are muscovite ($Kal_2(AlSi_3O_{10})(OH)_2$), PDF#00–058–2034), quartz (SiO_2, PDF#01–087–2096), potassium rich alkali-feldspars ($K_2O{\cdot}Al_2O_3{\cdot}6SiO_2$, PDF#00–019–0932), traces of kaolinite ($Al_2Si_2O_5(OH)_4$, PDF#04–013–3074), and an amorphous phase fraction distinguished by a very broad low intensity signal. C3, C4, and C5 have similar phase fractions of muscovite, quartz, and alkali-feldspar. C2 contains large quartz particles, small muscovite particles, and traces of anatase (TiO_2, PDF 01–086–1155), confirmed by the multimodal size distribution shown in Fig. 1 and SEM powder analysis shown in Fig. 3. C1 is the only sample to contain residual traces of kaolinite. The predominant crystalline phase in C1 is muscovite combined with its partially dehydroxylated form. Overlap between the main quartz peak ($\sim$ 27°) and the indexed muscovite pattern makes it difficult to determine whether quartz is in fact present in trace amounts.

The differences in particle size distribution and particle morphology between the calcined waste clay samples are highlighted in SEM images in Fig. 3.

C1 is composed of predominately small plate-like particles with a minor fraction of large particles present. C2 powder shows a similar multimodal distribution with distinct fine and coarse particle sizes. C3 and C5 have similar particle sizes but show differences in morphology. C5 has uniform plate-like particles, whilst C3 consists of plate shaped grains of various dimensions. C4 has the largest particle sizes among the calcined waste clays and exhibits regular equiaxed particle

Table 1
Density and particle size analysis of the precursors.

Sample	T calcination (°C)	Density (g/cm^3)	Particle size distribution (µm)		
			d_{10}	d_{50}	d_{90}
GGBFS	-	2.95	3.75	12.7	31.0
C1	800	2.59	2.72	10.5	263
C2	750	2.60	3.62	48.4	282
C3	800	2.61	7.85	26.2	77.0
C4	750	2.69	19.8	68.1	152
C5	800	2.69	8.15	24.5	66.0

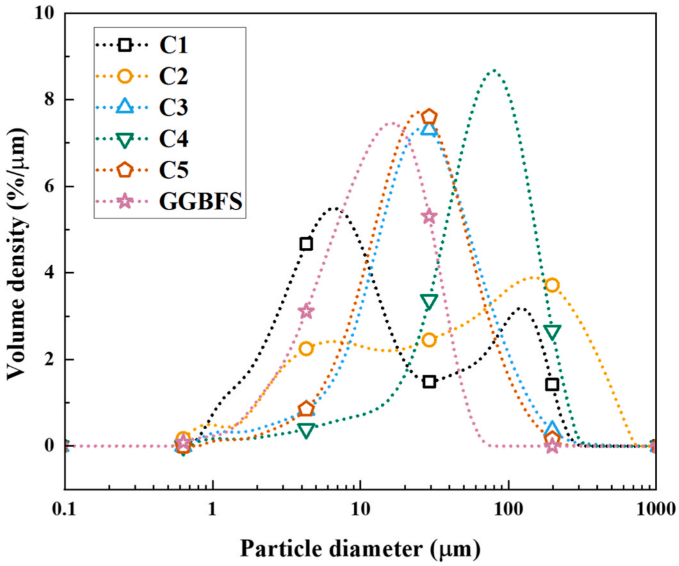

Fig. 1. Particle size distributions for calcined waste clays and GGBFS.

morphologies.

Fig. 4 shows the XRD patterns of C4 before and after calcination. The kaolinite content present in the uncalcined sample is dehydroxylated to form amorphous metakaolin in the calcined sample. The extent of structural order of muscovite is partially affected by calcination at 750–800 °C, as the peak intensities appear reduced when compared with the uncalcined sample. Dehydroxylation of muscovite is reported to proceed over a wide temperature interval via intermediate phases with noted changes in basal spacings following the progressive loss of water and transformation into a dehydroxylated phase [29]. There exists an increasingly disordered layered structure within the dehydroxylated phase that persists at high temperatures [30], with local structural order maintained between alumina and silica unit pairs [6]. The quartz present in C4 remains unaffected post-calcination. The chemical composition and structural parameters of the alkali-feldspar (K, Na)$_2$O·Al$_2$O$_3$·6SiO$_2$ phase present are not known. The combination of varying concentrations of K and Na within the structure and the newly formed phase from the dehydroxylation of muscovite both influence the phase peak positions in the XRD data, making it difficult to obtain structural parameters without more detailed compositional data. It was not possible to satisfactorily determine the phase factions of the crystalline/amorphous phases via Rietveld refinement due to the aforementioned ambiguities in compositional and structural parameters.

The thermogravimetric (TG) measurements were conducted by heating 20 mg of powder from 30 °C to 1000 °C at 10 °C/min, in an N$_2$ gas atmosphere. Fig. 5 shows the TGA data of uncalcined C4 waste clay. The major dehydroxylation peak associated with kaolinite is centred at 554 °C with a secondary peak at 629 °C. The content of metakaolin, assuming full dehydroxylation of kaolinite [31,32], is estimated to be approximately 30.8% considering the total mass loss between 450-750 °C attributed to the dehydroxylation of kaolinite.

2.2. Pozzolanicity tests

Pozzolanic reactivity of calcined clays refers to their ability to react with portlandite that is formed during the hydration of cementitious materials. Tests were based on a modified Chapelle test [33,34], measuring the amount of calcium hydroxide (Ca(OH)$_2$) fixed by the reaction of 1 g of calcined clay and 2 g of portlandite at 90 °C for 16 h. The portlandite content free in solution at the end of the reaction was extracted using sucrose and subjected to acid titration to determine its exact concentration. According to this test, the pozzolanic activity of a calcined clay source should not be less than 700 mg Ca(OH)$_2$/g metakaolin [33]. The results for the calcined waste clays (Table 3) show that 3 out of 5 samples are within this range, whilst the others are significantly below. Most surprising is the drop in pozzolanic reactivity seen in C4 compared to C3 and C5, even though all three samples show similar phase assemblage (Fig. 2) and particle morphologies (Fig. 3).

R3 tests [35] were performed to compare the chemical reactivity with pozzolanic activity data from the modified Chapelle test. Sieving clays may act to separate significant fractions of associated minerals, quartz and muscovite, with typically larger particle sizes that show limited reactivity, and eliminate any particle size effects on partial dehydroxylation of potentially reactive phases present. Using sieved fractions < 63 μm for the R3 test elucidates an indicative reactivity value achievable for processed calcined clays. The overall impact of this sieving step on reactivity is dependent on the particle size distributions which is expected to be more significant in the case of C4, exhibiting the

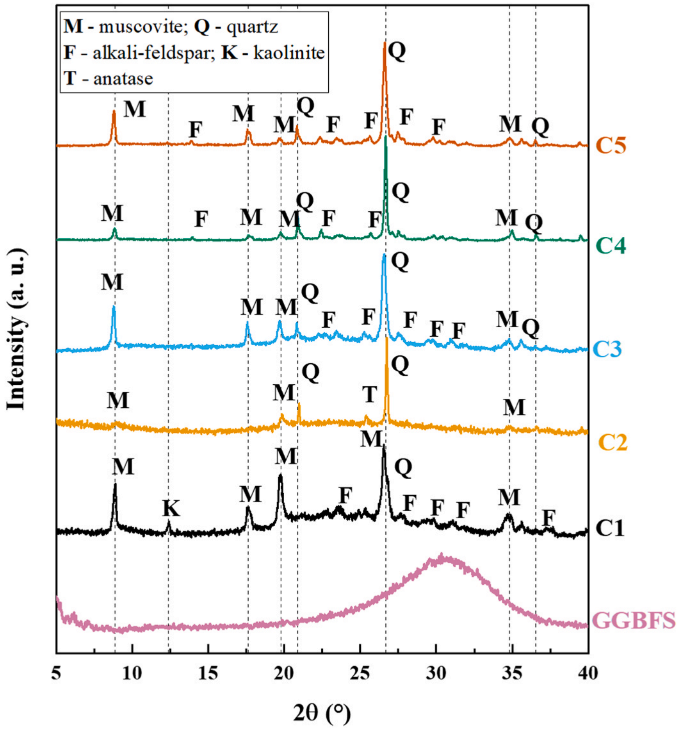

Fig. 2. XRD patterns of GGBFS and calcined waste clays.

Table 2
Chemical compositions of precursors (% oxide, by weight). L.O.I. is loss on ignition at 1000 °C.

Sample	SiO$_2$ (%)	Al$_2$O$_3$ (%)	CaO (%)	MgO (%)	Na$_2$O (%)	K$_2$O (%)	Cr$_2$O$_3$ (%)	Fe$_2$O$_3$ (%)	TiO$_2$ (%)	L.O.I.
GGBFS	36.4	10.5	43.5	7.0	-	-	1.4	0.3	0.5	0.2
C1	51.3	40.5	0.1	0.6	0.9	3.6	1.2	1.7	0.1	-
C2	54.4	41.5	0.1	0.2	0.2	1.2	1.2	1.5	0.8	-
C3	52.5	39.6	-	0.4	0.3	3.7	1.2	2.2	0.2	-
C4	66.6	23.6	0.1	0.4	0.4	5.0	1.3	2.4	0.2	-
C5	56.4	31.4	-	0.7	0.6	6.4	1.2	2.9	0.4	-

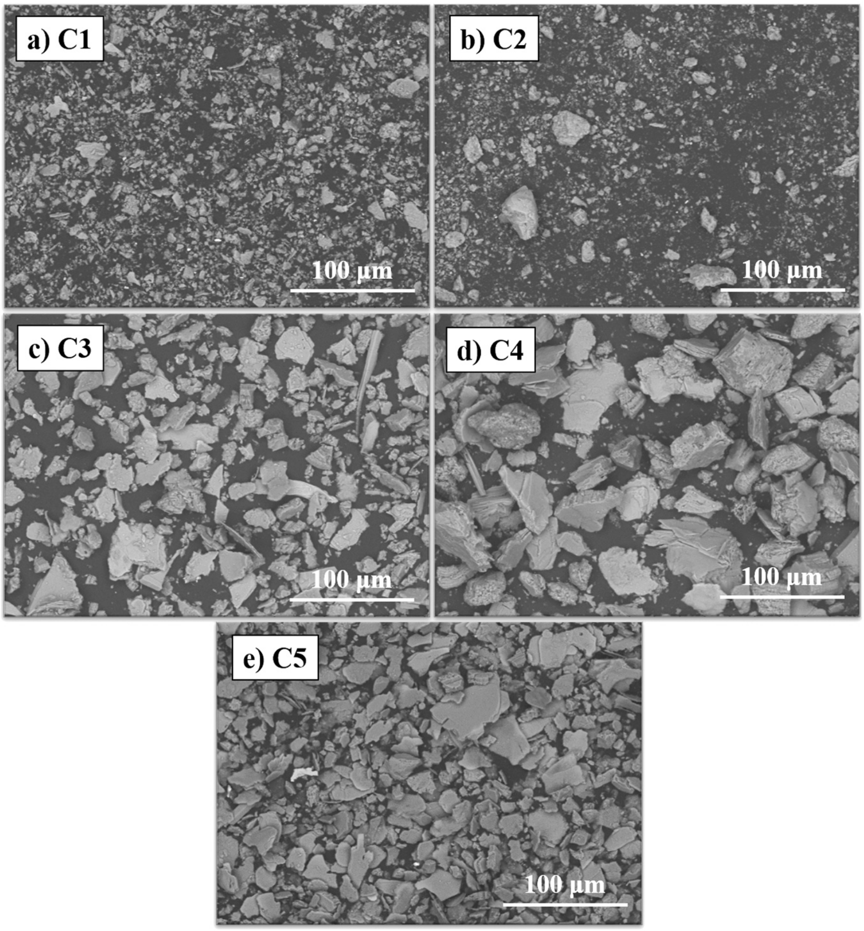

Fig. 3. SEM images of calcined waste clay samples C1 to C5.

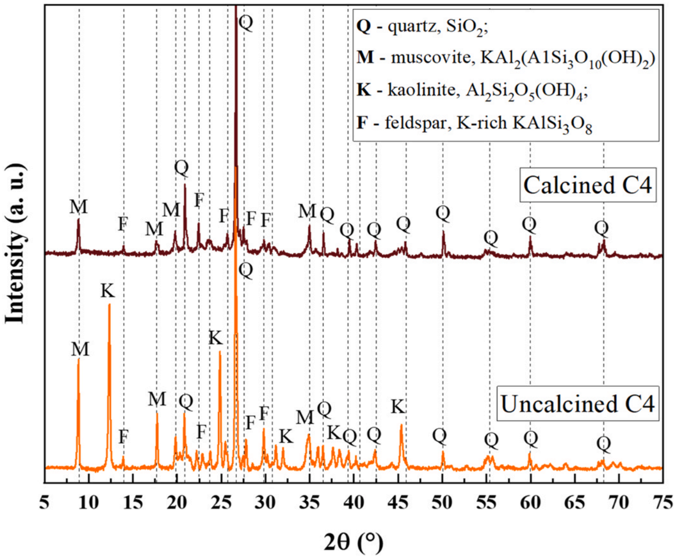

Fig. 4. XRD pattern of calcined waste clay C4 before and after calcination.

highest particle volume fraction > 63 µm out of the calcined clays (Fig. 1). The R3 test correlates pozzolanic activity with total heat released by the reaction of calcined waste clay, portlandite, and limestone pastes mixed with alkali-sulfates. Samples are hydrated for 6 days at 20 °C following the original methodology developed by Avet [35]. The results for the calcined waste clays are shown in Fig. 6. C1 shows the

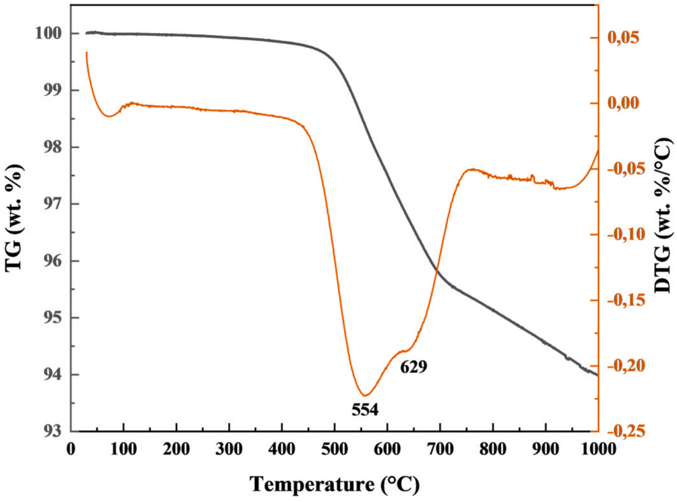

Fig. 5. TGA analysis of uncalcined waste clay C4 showing TG (left) and DTG (right) data.

highest reactivity, whilst C2 has the lowest recorded activity, in agreement with the modified Chapelle test data. The most noticeable difference is the now similar activity between C3, C4, and C5 samples.

The pozzolanic reactivity of calcined clays is not a direct measure of their reactivity in alkali-activation, where portlandite is absent. These tests are included in this work as potential indication of reactivity of calcined clays with the activator solution, as there is no specific direct

Table 3
Result of the modified Chapelle test to determine the pozzolanicity of the calcined waste clays.

Sample	mg Ca $(OH)_2$/g
C1	1011
C2	567
C3	967
C4	576
C5	943

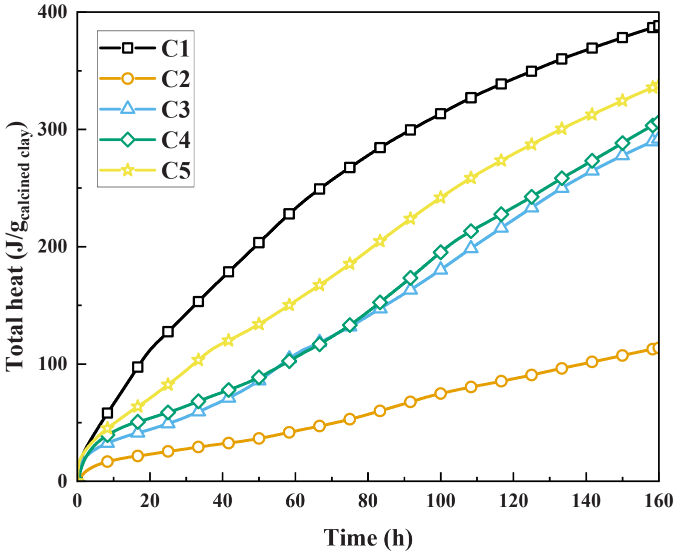

Fig. 6. Results of R3 test for calcined waste clays, based on the total heat released from a formulated paste during 6 days at 20 °C [35].

test for classifying their reactivity in alkali-activation. Reactive Si and Al in calcined clays may interact with alkaline solutions similar to the interaction with portlandite. The following results will suggest that a potential link between the reactivity of calcined clays in both alkali-activation and as SCM systems could exist, although it is crucial in alkali-activation to consider other factors, such as clay particle size, morphology, and mix design (including activator type, concentration, and blends with other solid precursors).

2.3. *Activator*

Sodium hydroxide (NaOH) pellets (purity > 98%, Sigma-Aldrich) and a commercial sodium silicate solution (PQ Silicates), with a solids content of 44.1% and a modulus (molar ratio SiO_2/Na_2O) of 2.07, were used to synthesis the alkaline activator solutions.

2.4. *Mix design and specimen preparation*

Alkali-activated pastes were initially prepared by mixing GGBFS with 30 wt% of each calcined waste clay to obtain five specimens with the same water/binder ratio and activator solution. The activator used for this study was a solution of sodium silicate with a modulus of 1.3 and 5.7 wt% Na_2O with respect to the sum of precursors (GGBFS and calcined waste clays), the amount of which was set to give a constant water/binder ratio of 0.4 for all five mixes.

The second part of this work investigated the effect of the activator solution, varying the modulus from 0.9 to 1.2 and the alkali dose (wt% Na_2O respect to all precursors) from 4.7 to 5.2 wt%, on blends based on 20 wt% C4 and 80 wt% GGBFS. The control formulation was designed on solely GGBFS to give the same Si/Al and Na/Al molar ratios as the calcined waste clay and GGBFS blend with lower activator dosage, designated type “a”. A water-to-binder ratio of 0.38 was maintained constant across all three mixes.

All pastes were mixed using a Kenwood planetary mixer. The precursors were intially dry mixed for 60 s to achieve an even distribution. Subsequently, the alkali solution prepared 24 h in advance was introduced to the mixer for 30 s, followed by 2 min at low speed (140 rpm) and 3 min high speed (400 rpm) to achieve a homogenous mixture.

Binder formulations are given in Table 4.

2.5. *Testing methods*

2.5.1. *Isothermal calorimetry*

The reaction kinetics of pastes were investigated using an isothermal calorimeter TAM Air (TA Instruments, USA) collecting measurements at 20 °C. 20 g of solid precursors were transferred into a glass ampoule after mixing for ~ 2 min. After sealing, the ampoule was immediately transferred into the machine along with a reference sample of a corresponding mass of water, which was measured following the procedure described by Wadsö [36]. The duration of measurement spanned two weeks. All values of heat release rate were normalised according to the total weight of solid binder.

2.5.2. *Setting time*

The Vicat technique was used to evaluate initial and final setting times of fresh alkali-activated pastes, with experiments performed in an automatic Matest VICATRONIC apparatus (Impact Test Equipment, UK) equipped with a 1.13 mm needle, following the standard testing procedure EN 196–3 [37] considering the nature of the materials being tested. Fresh pastes were poured into a conical frustum mould with a height of 40 mm, top internal diameter of 60 mm, and bottom internal diameter of 70 mm. The initial setting time was determined as the moment in which the separation between the needle and the base plate reached 6 ± 3 mm. The final setting time was recorded once a maximum penetration depth of 0.5 mm into the specimen was achieved.

2.5.3. *Mini-slump tests*

A mini-slump test was conducted on fresh mixtures after 30 min to determine paste workability. A slump cone with a height of 40 mm, and internal top and bottom diameters of 38 and 60 mm respectively was used. For each slump test, the slump cone was placed on a flat sheet and gradually filled with the fresh mixture. The cone was then lifted slowly (< 1 cm/s) [38] and the mean value of the flow diameters measured in two perpendicular directions recorded as the spread.

2.5.4. *X-ray diffraction (XRD)*

XRD analysis was performed using a PANalytical X'Pert^3 (PANalytical, USA) diffractometer operating in Bragg-Brentano geometry with a Cu Kα radiation source at 45 kV and 40 mA, fitted with a PIXcel-Medipix3 detector. Samples were analysed between the 2θ range of 5–60°, using a step size of 0.02°. Phase identification was carried out

Table 4
Mix proportions of alkali-activated blends using GGBFS and calcined waste clays C1 to C5.

Sample	Precursors		Activator solution		w/b mass ratio
	Calcined waste clay	GGBFS	Modulus (MR SiO_2/Na_2O)	Alkalinity (% Na_2O)	
30C1	C1: 30 wt%	70 wt%	1.3	5.7	0.4
30C2	C2: 30 wt%	70 wt%	1.3	5.7	0.4
30C3	C3: 30 wt%	70 wt%	1.3	5.7	0.4
30C4	C4: 30 wt%	70 wt%	1.3	5.7	0.4
30C5	C5: 30 wt%	70 wt%	1.3	5.7	0.4
0C4-a	-	100 wt %	0.6	4.0	0.38
20C4-b	C4: 20 wt%	80 wt%	0.9	4.7	0.38
20C4-c	C4: 20 wt%	80 wt%	1.2	5.2	0.38

using ICDD PDF+ 4 (ICDD, USA) and HighScore plus (Malvern Panalytical, UK).

2.5.5. *Fourier-transform infra-red (FTIR)*

FTIR analysis was performed using a PerkinElmer Frontier FTIR spectrometer (PerkinElmer, USA). 2 mg of precursor material were mixed and ground together with 200 mg of KBr. The mixed powder was transferred to a 13 mm pellet die and pressed with a10 tonne-force to a form a transparent pellet which was subsequently tested in the spectrometer. FTIR spectra were collected between 4000 and 400 cm^{-1}, with a resolution of 2 $cm^{-1,}$ averaged over 32 scans.

2.5.6. *Solid-state nuclear magnetic resonance (NMR)*

Solid state single pulse ^{27}Al and ^{29}Si magic angle spinning (MAS) NMR spectra were acquired on a Bruker Avance III HD 500 spectrometer at 11.7 T (B0) using a 4.0 mm dual resonance CP/MAS probe, yielding a Larmor frequency of 130.32 MHz for ^{27}Al and 99.35 MHz for ^{29}Si. ^{27}Al MAS NMR spectra were collected using 1.7 µs nonselective ($\pi/2$) excitation pulse, a spinning speed of 12.5 kHz, 5 s relaxation delay, for a total of 512 scans, and were qualitatively interpreted. ^{29}Si MAS NMR spectra were acquired using a 5.5 µs nonselective ($\pi/2$) excitation pulse, a spinning speed of 12.5 kHz, 60 s relaxation delay, for a total of 256 scans. Gaussian curves were used to deconvolute the ^{29}Si MAS NMR spectra, fitting the minimum number of peaks and maintaining consistent the peak position and full width at half maximum (FWHM) of each resonance. The chemical shifts were compared to an external standard of 1.0 M Al(NO3)3 for all ^{27}Al spectra and to pure tetramethylsilane (TMS) for ^{29}Si spectra. All analysis was performed using Bruker Top Spin 4.0.

2.5.7. *Scanning electron microscopy (SEM)*

Scanning electron microscopy (SEM) was conducted using Hitachi TM3030 instrument coupled with the EDS (Energy-dispersive X-ray spectroscopy) software Bruker QUANTAX 70. Powder specimens were prepared by placing a small amount of powder material on a carbon dot adhered to a 12.5 mm Al SEM pin stub. Loose powder was removed using compressed air. Hardened paste fragments were mounted in epoxy resin, left to cure overnight, and demoulded ready for polishing. Samples were polished using SiC sandpaper in ascending grits, and carbon coated prior to SEM analysis.

2.5.8. *Compressive strength*

Compressive strength tests were carried out using a Shimadzu 300 kN compression testing machine applying 1200 N/s. Paste specimens were tested according to relevant sections of the ASTM C109 [39] standard adapted for use with AACs, consisting of 50 mm cubes, demoulded after one day, and then sealed and cured in an environmental chamber at 20 ± 1 °C and relative humidity of 45 ± 1% until reaching designated testing ages (7 and 28 days). The strength values for the mixtures at each testing age are reported as the mean value of three tests.

2.5.9. *Mercury intrusion porosimetry (MIP)*

The porosity of samples was analysed via MIP tests. Prior to analysis the specimens were crushed into 10 mm pieces and immersed in isopropanol for two days in order to stop the hydration process. Preserved specimens were then dried at 35 °C and stored under vacuum at ambient temperatures for one week. MIP measurements were carried out using an AutoPore V (Micrometrics, UK) porosimeter. Pieces of ∼ 10 mm size were selected to give a total charge of 2.2 ± 0.2 g. The mercury/material contact angle was set to 130° [40]. The analysis was conducted with a gradual reduction of pressure (up to 50 µHg) and a surface tension of mercury of 0.485 N/m was used in the calculations. Pore size and volume were measured at ∼ 200 mPa.

3. Results and discussion

3.1. *Alkali activated blends of GGBFS and 30 wt% of calcined waste clays*

3.1.1. *Isothermal calorimetry*

Isothermal calorimetry experiments were carried out to determine the reaction kinetics of blended mixes. Fig. 7(a) shows the heat flow developed by the five alkali-activated mixtures with different calcined waste clays. The general reaction occurs in two stages, identified by the appearance of two exotherms in the calorimetry data. The first stage (I) takes place from the onset of reaction lasting up to ∼ 5 h. This initial heat release is associated with wetting and dissolution of reactive precursor material and an initial formation of reaction gel products [41]. The intensity of this initial exotherm is similar across all mixes except for 30C2 and 30C5, reaching a maximum around 1 h. The initial exotherm for the 30C2 mix has a lower intensity and is slightly delayed compared to the other mixes. The relative intensity of the initial exotherm for 30C2, related to the degree of wetting and dissolution, is reflective of the stability of quartz in alkaline environment [42], identified as the predominant crystalline phase in C2 from XRD data. Differences across the calcined waste clays may indicate variations in the availability and reactive nature of Si and Al phases present in each sample in alkaline environments [43]. This stage is followed by a dormant period during which the rate of heat evolution is low but non-zero. The dormant period appears brief for all mixtures except 30C2 which is noted to have the lowest pozzolanic reactivity (Table 3). The second reaction stage (II) is attributed to polycondensation, further nucleation and growth of gel reaction products, from 5 to 60 h. The appearance of this stage (II) exotherm is associated with the formation of more ordered C-A-S-H and N-A-S-H gels [44]. Many factors affect the (II) exotherm stage, however, having the same level of alkalinity in all systems, the high intensities shown by 30C5 and 30C4 might be the result of availability of Si and Al from the calcined waste clay resulting in large amounts of reaction products [43]. This second exotherm is not seen in the 30C2 mix, suggesting minimal gel condensation and transformation attributed to a clear lack of reactivity at early ages. Initial limited gel formation is not followed by significant transformation into a more ordered gel structure. The intensity and timing of this second exotherm follows the general trend in pozzolanic reactivity seen in the R3 test (Fig. 6). With the exception of C1, the more reactive calcined waste clays show more intense second exotherms at shorter reaction times. The lower than expected heat release recorded for 30C1 is attributed to the formation of microstructural clusters that can hinder ideal reaction kinetics, and is further discussed in the following sections. After deceleration of the second exotherm, the reaction enters into a steady state in which minimal heat is continuously released as the reaction proceeds.

Fig. 7(b) illustrates that after a reaction time of 150 h, the total heat evolved for 30C1, 30C3, 30C4, and 30C5 is in a similar range, whilst the total heat release by the 30C2 mix was approximately half that of the other mixes. Over time, it becomes apparent that the total heat evolution curve for the 30C1 mix surpasses that of the 30C4 mix as particle agglomeration becomes less of a limitation to reaction, enabling the higher pozzolanic reactivity of the C1 material to be fully realised.

Within the investigated systems, a consistently elevated level of alkalinity persists throughout the entirety of the reaction process. This high alkalinity provides the necessary conditions to drive the dissolution of metakaolin contained in the calcined waste clays [15].

3.1.2. *Setting time and mini-slump tests*

Table 5 displays the initial and final setting times for all mixtures containing 30 wt% calcined waste clays. The range of values across all calcined waste clay mixes is quite narrow, spanning from 80 to 170 min

Previous studies report that the incorporation of metakaolin into slag systems can result in prolonged setting times [28,45], although the opposite effect has been reported with increasing activator dosage [24,

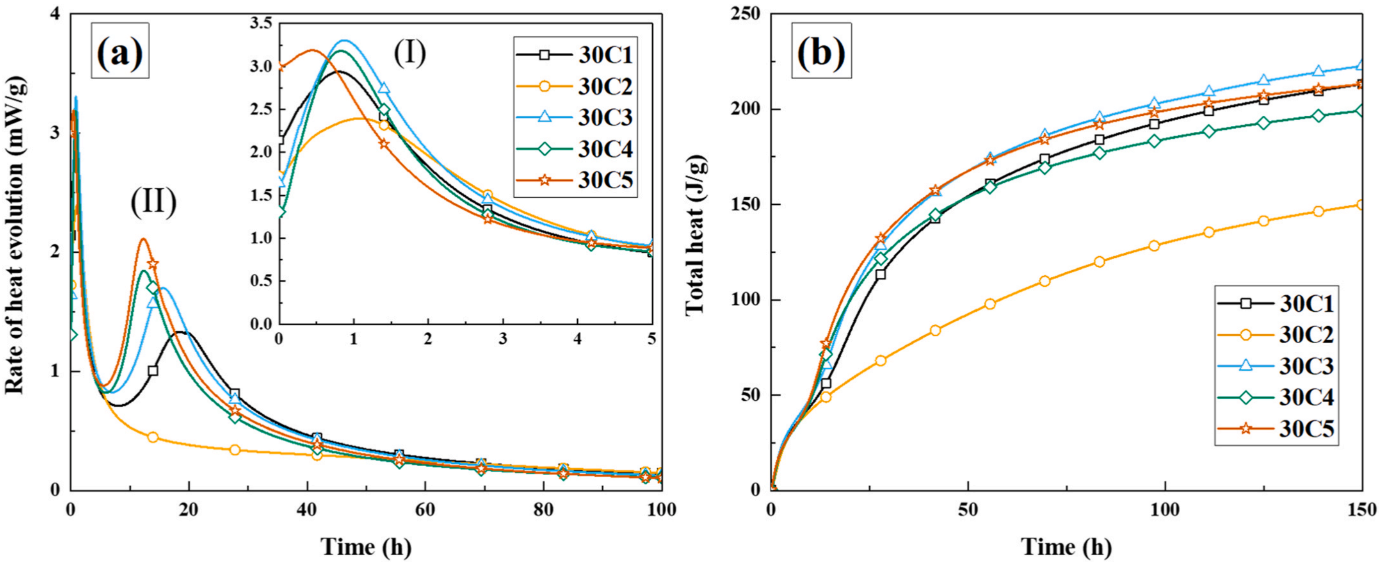

Fig. 7. (a) Rate of heat evolution and (b) cumulative heat of alkali-activated blends of 30 wt% calcined waste clays/70 wt% GGBFS, at 20 °C.

Table 5
Initial and final setting times for alkali-activated paste samples including 30 wt % calcined waste clay and 70 wt% GGBFS.

Sample	Setting time (min)		Mini-slump diameter (mm)
	Initial	Final	
30C1	100	140	75
30C2	110	150	105
30C3	120	160	97
30C4	120	170	132
30C5	80	120	100

46] due to the increased dissolution rate of Si and Al species from metakaolin in high pH systems [47]. The results in this study align with the latter observation, as evidenced by the relatively short setting times. In particular, the 30C5 mixture exhibits the fastest initial and final setting times of 80 min and 120 min, respectively. This supports the understanding that C5 contains high amounts of reactive Si and Al, as indicated by the calorimetry data in 3.1.1, which may be associated with a large metakaolin fraction.

Mini-slump test results indicate a range from 75 mm (30C1) to 132 mm (30C4), noting that the original cone base diameter (i.e. the zero slump measurement) is 60 mm. Particle size distribution is an important factor determining workability, with larger particle size distributions showing improved flow and lower water demand in mix designs [48]. The trend in slump values seen in Table 5 agrees with the particle size data reported in Table 1, with larger particle sizes resulting in greater slump values. Particle morphology, especially in the case of metakaolin which has been reported to lower workability due to its distinct plate-like particle morphology [49], may also affect slump results. Large particle surface area to volume ratios may increase the opportunity for inter-particulate forces, such as van der Waals forces, to form agglomerates upon particle collisions [50] by disrupting the uniformity of particle double layers and promoting electrostatic interactions [51].

3.1.3. *X-ray diffraction*

Fig. 8 displays the XRD patterns of alkali-activated blends of GGBFS with 30 wt% calcined waste clays. The formation of multiple new phases during alkali activation is evident upon comparison with the XRD patterns of both calcined waste clays and raw GGBFS shown in Fig. 2. The presence of calcite ($CaCO_3$), which displays a prominent peak at approximately 29° 2θ, hydrotalcite characterised by distinct broad peaks around 11° 2θ, and C-S-H (or C-A-S-H) identified by broad peaks at approximately 29° and 50° 2θ, can be observed in all of the alkali-activated blends investigated; these phases are generally associated with the alkali-activation of GGBFS [52]. The main difference between the calcined waste clays is seen in the 30C2 pattern which exhibits a markedly reduced intensity of the broad C-S-H peak. The low gel phase fraction is expected, as evidenced by the suppression of the secondary polycondensation exotherm in the calorimetry data shown in Fig. 7. Muscovite, quartz, and alkali-feldspar are seen in the XRD patterns as remaining components of the calcined waste clays. It cannot be ruled out that the dehydroxylated fraction of muscovite has undergone some form of reaction, however it is clear that unreacted muscovite persists (Fig. 8). Temperatures > 800 °C are reported to be necessary for complete transformation [29,53], and the distinction between the hydroxylated and dehydroxylated forms of muscovite is non-trivial from XRD data [54]. The K-feldspar may also slowly release alkalis in highly alkaline

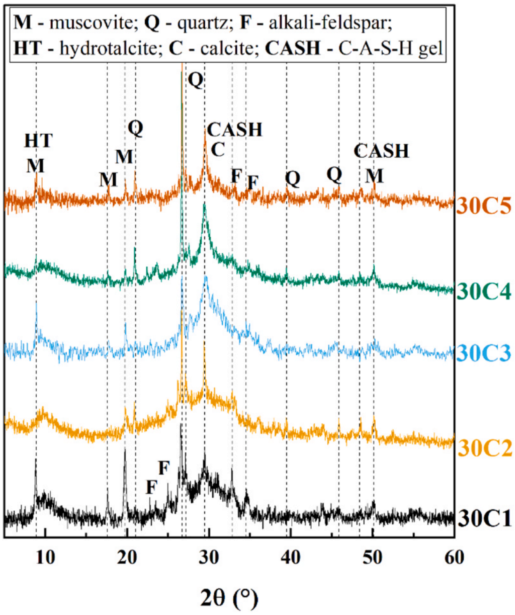

Fig. 8. XRD patterns of alkali-activated blends with 30 wt% of calcined waste clays after 28 days.

environments, however this effect is not easily determined [55–57].

3.1.4. Scanning electron microscopy

Backscattered electron (BSE) images of alkali-activated blends of GGBFS and 30 wt% calcined waste clays after 28 days are shown in Fig. 9. The brightest Z-contrast particles seen in all samples are identified as unreacted GGBFS due to the presence of Ca, as seen in the EDS spot analysis corresponding to one such particle. Ca is not expected to be present in significant quantities in the calcined waste clay particles. Unreacted GGBFS is surrounded by a gel matrix phase, consisting of predominantly C-(A)-S-H gel, that also encapsulates the associated mineral phases present in the calcined waste clays. Each sample shows distinctive particles with varying Z-contrast, representative of the differing composition of each mineral phase.

Fig. 9(a) shows a large agglomerate of small clay (C1) particles within the gel matrix. The presence of high remnant porosity in this agglomerate indicates poor particle wetting by the activator solution, which if found throughout the specimen would result in less dissolution and polycondensation reactivity. This lack of reactivity is observed as lower heat evolution during the reaction, as shown in Fig. 7. These defects which are seen all across the specimen might be responsible for the disparity between pozzolanic reactivity (Table 3), determined under near ideal conditions, and mix reaction kinetics (Fig. 7), which are heavily influenced by the completeness of wetting of agglomerated particles, and thus the relative ability to reach homogenous mixing. These porous regions are expected to be relatively mechanically weak and vulnerable to crack formation and propagation compared to the bulk binder. Therefore, it is crucial to take extra precautions to ensure complete mixing [58], particularly in cases where small particle sizes and high electrostatic interactions promote cluster formation. In the case of 30C2, a clear reduction in overall gel phase fraction is seen by the large number of both fine and coarse unreacted GGBFS particles throughout the matrix in Fig. 9(b). The interparticle spacing between GGBFS particles is substantially smaller than is seen in the other samples, indicating a lack of enhanced gel formation as observed from the complete suppression of the secondary exotherm in the 30C2 calorimetry data (Fig. 7). Around both agglomerate phases identified in Fig. 9(a and b), an N-A-S-H phase with low calcium content is slowly forming as determined from EDS. The presence of calcium in the N-A-S-H gel suggests that calcium from the GGBFS diffuses into the gel, consistent with reported findings [18,59].

Conversely, the chemical composition of the bulk reaction products exhibited high concentrations of Si, Ca, Al, and Na, indicating the formation of a C-A-S-H gel with Na^+ partially absorbed into the interlaminar space of the structure, (C-(N-)A-S-H). Associated minerals such as muscovite, quartz, and feldspar can be distinguished in the 30C3, 30C4,

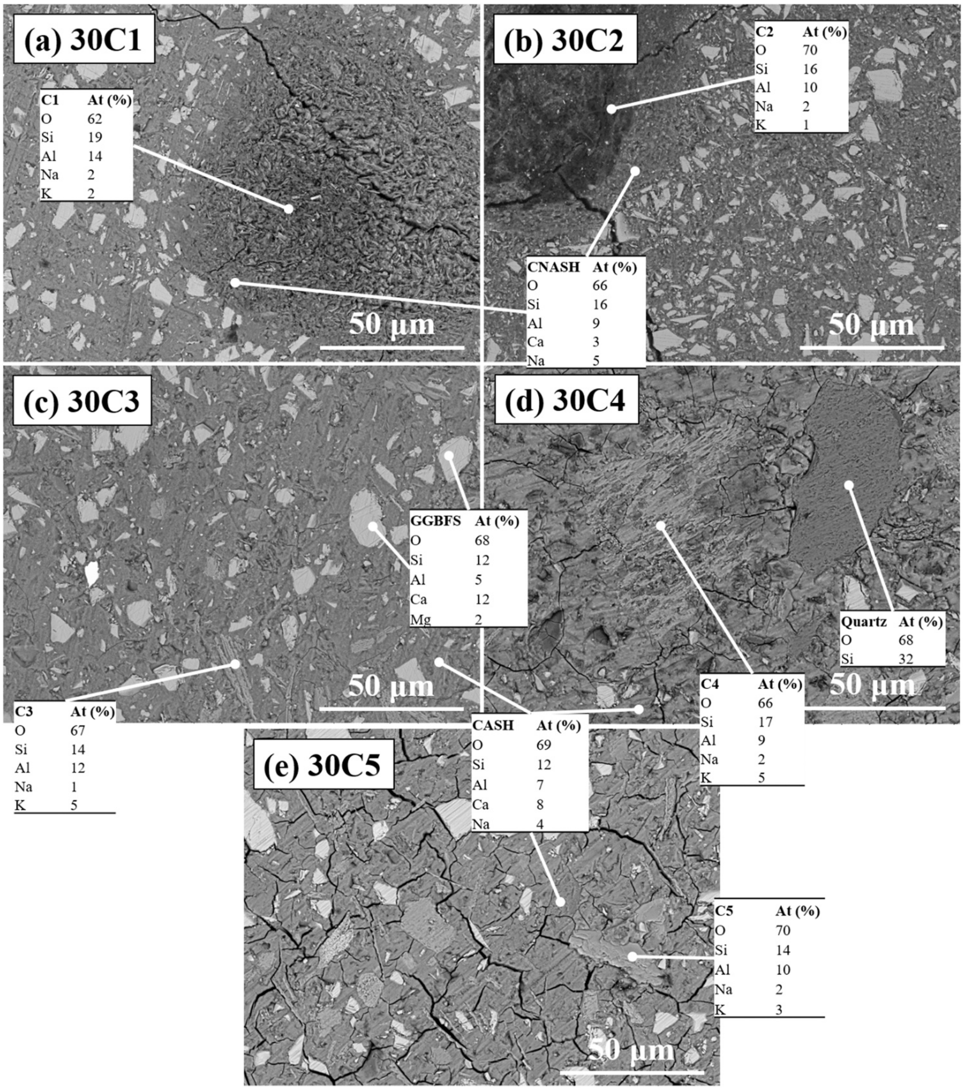

C1	At (%)
O	62
Si	19
Al	14
Na	2
K	2

C2	At (%)
O	70
Si	16
Al	10
Na	2
K	1

CNASH	At (%)
O	66
Si	16
Al	9
Ca	3
Na	5

GGBFS	At (%)
O	68
Si	12
Al	5
Ca	12
Mg	2

Quartz	At (%)
O	68
Si	32

C3	At (%)
O	67
Si	14
Al	12
Na	1
K	5

CASH	At (%)
O	69
Si	12
Al	7
Ca	8
Na	4

C4	At (%)
O	66
Si	17
Al	9
Na	2
K	5

C5	At (%)
O	70
Si	14
Al	10
Na	2
K	3

Fig. 9. Backscattered electron (BSE) images of alkali-activated blends of GGBFS and 30 wt% calcined waste clays after 28 days of curing. EDS values are included for particles and characteristic features and calculated as an average of at least five points. (Error ± 1%).

and 30C5 microstructures surrounded by a dense gel matrix (Fig. 9(c, d, e)). The varying Z-contrast of the mineral particles combined with EDS analysis allow for identification of the unreacted mineral phases present, with the most prominent being elongated muscovite and alkali-feldspar particles seen in Fig. 9(c), and a large quartz particle in Fig. 9(d)], consistent with the XRD data discussed in Section 3.1.3.

3.1.5. *Compressive strength*

The compressive strength results for the alkali-activated blends, as seen in Fig. 10, can be categorised into two general groups: group (I) including both 30C1 and 30C2 which achieve compressive strengths of < 40 MPa after 7 days, and group (II) including 30C3, 30C4, and 30C5 which develop similar compressive strengths of around 60 MPa after 7 days.

All samples show an increase in compressive strength from 7 to 28 days, with 30C5 attaining a maximum compressive strength of 80 MPa. Out of the group (II) samples, 30C4 shows the lowest compressive strength gain from 7 to 28 days. The high early strength exhibited by 30C4 can be ascribed to combinations of physical effects such as dilution and nucleation effects [60]. This is attributed to the substantial presence of unreactive quartz in C4, which promotes a higher degree of polycondensation of GGBFS and metakaolin within C4, increasing the activator availability per unit mass. As a result, a more efficient paste product is formed at early ages. This also explains the limited increase in strength observed from 7 to 28 days, as physical effects are likely to be noted in the initial stages [60]. The improved flow and dispersion characteristics of group (II) calcined waste clays, as seen in the mini-slump tests (Table 5), contributes to the development of a dense microstructure that underpins higher compressive strengths. The partial amorphous content in these calcined waste clays is believed to react during alkali activation to provide a greater volume fraction of binder phases. In group (I), the lower compressive strength of 30C1 in spite of the high pozzolanic reactivity of the C1 clay is explained in terms of the poor mixing and dispersion issues highlighted by lower workability (Table 5) and visible microstructural defects in Fig. 9(a). The poor pozzolanic reactivity of C2 has a detrimental effect on the achieved compressive strength of 30C2 due to reduced gel phase formation. Clearly the dispersion and homogenisation of precursors during mixing is a key factor in producing optimised blends, which if overlooked, can result in the discrepancies between high initial precursor reactivity and low compressive strengths seen here.

The current results are comparable with previous studies investigating 50 wt% pure metakaolin and GGBFS with similar activator concentrations (modulus 1.5 and alkaline dosage of 5 wt%) reporting a compressive strength of 80 MPa after 28 days [18]. Increasing the GGBFS content to 70 wt% effectively compensates for the lower metakaolin content of the calcined waste clays. This is clearly supported by the fact that the compressive strength achieved by group (II) aligns closely with the results reported in [18], whilst for group (I), the deviation from these results confirms that the issue extends beyond just the low metakaolin content, as their results fall below 50 MPa.

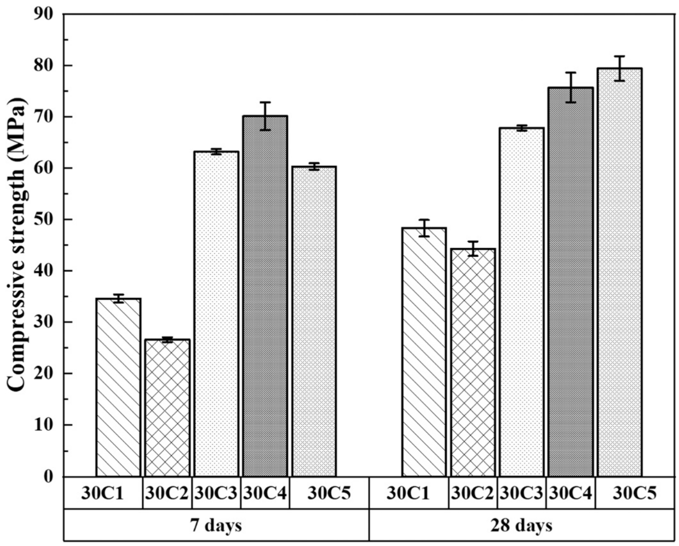

Fig. 10. Compressive strength of alkali-activated blends of 30 wt% calcined waste clays and GGBFS after 7 days and 28 days.

3.2. *Proof of concept: developing a blended binder with 20 wt% calcined waste clay C4 maintaining comparable properties to a solely GGBFS binder*

The current expectation from the concrete industry is that calcined clay replacement fractions in cements do not greatly exceed 20 wt% due to operational limitations, and to excessive shrinkage and porosity, and strength reduction [61]. Thus, 20 wt% replacement of GGBFS with calcined waste clay C4 was selected for further investigation of the effect of varying the modulus of sodium silicate activator solutions compared to an unblended GGBFS-based system. Achieving satisfactory mixing properties is also a key factor in further upscaling blended mixtures [62], and for this reason C4 was selected. The mix designs are described in Table 4.

3.2.1. *Isothermal calorimetry*

The heat evolution profiles of alkali activated GGBFS, and 20 wt% C4 / 80 wt% GGBFS blends varying the modulus of the activator solution, are shown in Fig. 11 (a). The large exotherm seen before 5 h in all mixes is identified as the pre-induction period representing wetting of the solid precursors followed by initial particle dissolution and gel formation [63]. This first stage (I) is followed by an induction or dormant period characterised by a low but non-zero rate of heat release in which the dissolution process continues [63]. The presence of an induction period in slag-rich AACs is characteristic of sodium silicate activated systems rather than systems activated purely by sodium hydroxide [44]. The 0C4-a sample has a relatively short induction period of ~10 h followed by a second exotherm with a maximum rate of heat release recorded at 15 h. This second reaction stage (II) is again (as discussed in Section 3.1.1) associated with the precipitation, nucleation, and growth of reaction gel products during polycondensation [63,64]. Sample 0C4-a shows reaction acceleration and deceleration all within the space of 24 h. Data obtained for the 20C4-b and 20C4-c mixes show profiles with two distinct exotherms, similar to 0C4-a. The initial exotherms are more intense with a higher activator modulus giving the presence of reactive dissolved Si species, and slightly broader implying a longer dissolution period of the less reactive C4 component. The second stage exotherms of 20C4-c and 0C4-a are remarkably similar in intensity, albeit with a broader acceleration deceleration period for 20C4-c concluded within 48 h, suggesting that the increase in modulus between activators “a” and “c” may compensate for the lower reactivity of the calcined waste clay than GGBFS. The 20C4-b sample exhibits a much longer induction period of ~16 h before the second exotherm. The second stage is again slightly depressed in intensity and broader, reaching a steady state after 50 h with both 0C4-a and 20C4-c, explained by the reduced availability of initial reactive gel-forming species present within the system when replacing GGBFS with C4.

These observations on reaction kinetics of these binders are agreement with previous studies on sodium silicate activated slags [63,65] and GGBFS systems activated by mixtures of sodium hydroxide and sodium silicate [66] that report two exotherms separated by an induction period. The inclusion of calcined waste clay prolongs the overall dissolution period, highlighted by a general broadening of the exotherms. It is interesting to notice in Fig. 11 (b) that after ~50 h of reaction the total heat released by both 20C4-b and 20C4-c is in fact larger than 0C4-a.

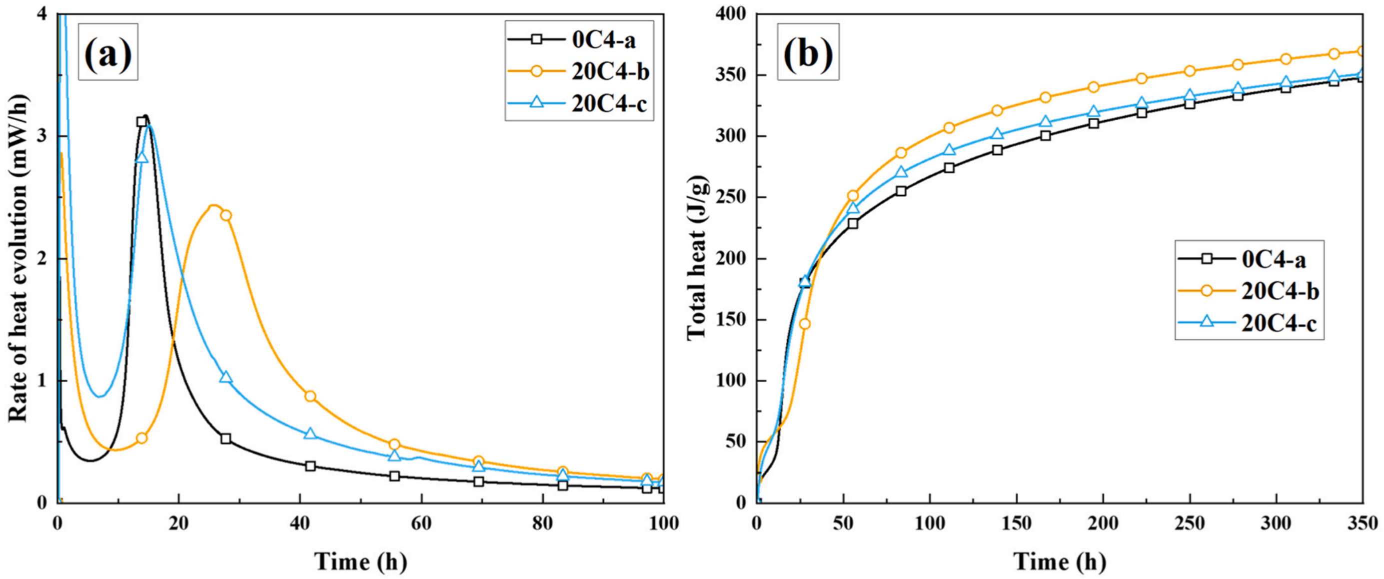

Fig. 11. (a) Heat evolution and (b) cumulative heat of alkali-activated blends of 20 wt% C4 and 80 wt% GGBFS, reacting at 20 °C.

3.2.2. *Setting time and mini-slump tests*

The blended systems 20C4-b and 20C4-c exhibit faster initial and final setting times than 0C4-a. This could be simply explained on the basis of increasing activator concentration. However, the inclusion of C4, known to contain an amorphous metakaolin fraction, may also enable synergistic effects between its reactive metakaolin component and the Ca-rich GGBFS to accelerate the reaction and lower the setting time [67]. Table 6.

Mini-slump results show an increase in workability of around 40% with C4 inclusion and increased activator concentration. This effect can be explained by the morphology of the C4 particles, predominantly large and equiaxed particles (d_{50} ∼ 68 μm) which are much larger than the GGBFS particles (d_{50} ∼ 12 μm) and undergo greater dispersion during mixing (Fig. 1). It is known that smaller particles have an increased tendency to flocculate due to high surface area and increased weak physical interactions; the resulting dispersion problems are usually alleviated by either an increase in water content or the addition of a superplasticizer [68].

3.2.3. *X-ray diffraction*

Fig. 12 shows the XRD patterns for the alkali activated mixes. The pattern for 0C4-a shows distinct amorphous humps centred in ∼7°, ∼ 29°, ∼ 32° and ∼ 50° 2θ indicative of C-S-H/C-A-S-H gel formation [69]. The minor crystalline phase identified is a hydrotalcite-group phase (HT) which has been studied extensively in alkali-activated slag systems [70–72]. The formation of hydrotalcite-group phases involves the dissolution of Mg^{2+} present within GGBFS, and precipitation with recrystallisation. The inclusion of hydrotalcite is known to impart beneficial properties on overall binder behaviour including resistance to carbonation and chloride ingress [66,73].

The primary crystalline phases of the precursor calcined waste clay C4 – muscovite (M) and quartz (Q) – are present throughout the 20C4-b and 20C4-c patterns obtained after 2, 28, and 90 days. Again the broad response at ∼ 29° 2θ highlights the formation of C-S-H/C-A-S-H gel after alkali-activation. The formation of hydrotalcite in the 20C4-b mix is seen after 2 days, but hydrotalcite formation is barely detected in the 20C4-c pattern. The higher activator modulus is expected to limit the degree of XRD-observable HT formation, with much smaller HT precipitates (nanoscale) favoured in higher modulus environments [74].

Table 6
Mini-slump tests and initial and final setting time results for alkali-activated blends of 20 wt% C4 and GGBFS.

Sample	Setting time (min)		Mini slump
	Initial	Final	mm
0C4-a	200	280	92
20C4-b	145	265	129
20C4-c	125	180	132

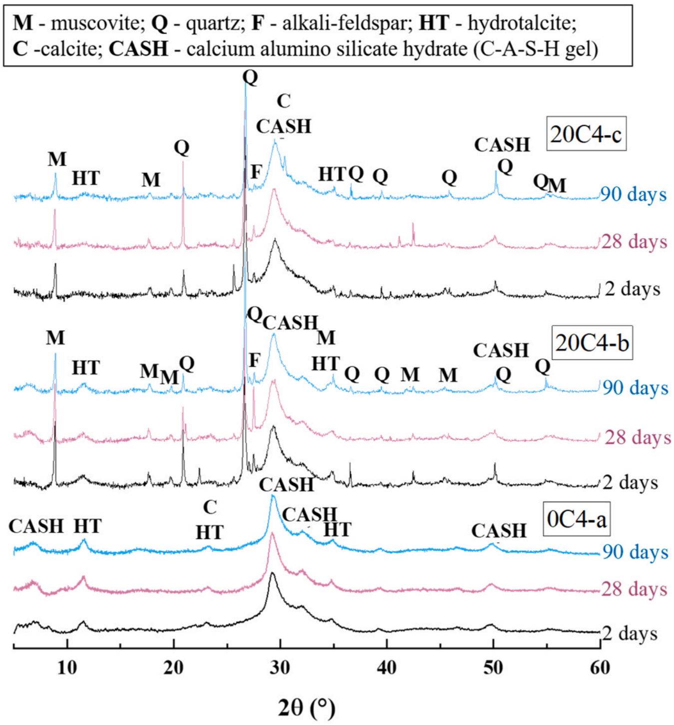

Fig. 12. XRD patterns of alkali-activated GGBFS (0C4-a), and blends of 20 wt% C4 and 80 wt% GGBFS (20 C4-b and 20C4-c).

3.2.4. *Fourier transform infra-red spectroscopy*

FTIR spectra of raw GGBFS, calcined waste clay C4, and the alkali-activated pastes 0 C-a, 20C4-b, and 20C4-c after 2 and 28 days, are displayed in Fig. 13.

The GGBFS absorption spectrum shows a major absorption band with

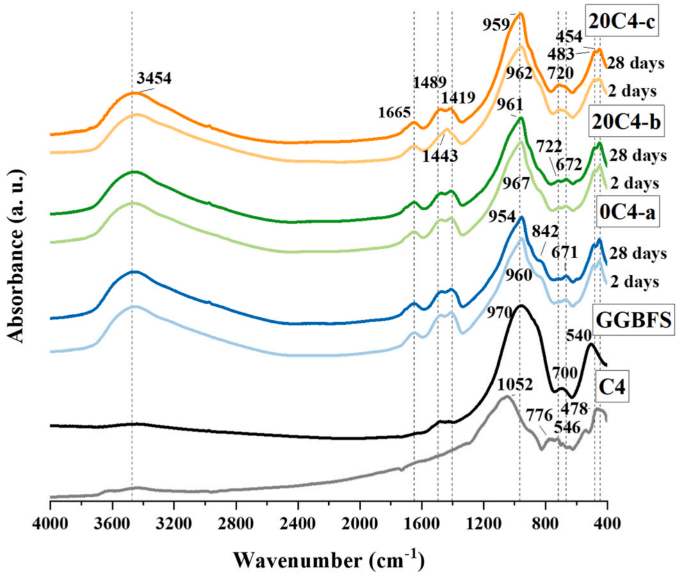

Fig. 13. FTIR spectra of precursors and alkali-activated samples based on GBBFS with and without 20 wt% C4, after 2 and 28 days of curing.

a peak at ~ 970 cm^{-1} relating to asymmetric silicate (Si-O-T, with T = tetrahedral Si, Al) bond stretching vibrations, whereby the stretching of the Si tetrahedron in question results in a simultaneous contraction of adjacently bonded tetrahedral Si or Al, i.e. opposite atomic motion [75]. The absorption band ~ 700 cm^{-1} is due to symmetric Si-O-Si bond stretching along with the final absorption band ~ 540 cm^{-1} indicative of Si-O-T bond bending [76,77]. C4 has a main band with centred around 1052 cm^{-1} indicative of bonding vibrations Si–O-T seen in quartz, but also in metakaolin, which is responsible for the broadness of this band [78]. Other bands at 776 cm^{-1}, attributed to the Al–O bending of AlO_6 octahedral sites within metakaolin [79], at 546 cm^{-1}, and 478 cm^{-1} can be attributed to crystalline quartz and muscovite [80].

Looking at the absorption spectra obtained for the alkali-activated specimens, the first absorption band ~ 3454 cm^{-1} is due to H-O-H bond stretching from weakly bonded water molecules trapped on the surface or in pores within the samples, along with the corresponding H-O-H bond bending at ~ 1655 cm^{-1} [77,81]. The bands between 1490 and 1410 cm^{-1} are related to O-C-O bond stretching [82,83]; in particular the absorption peak ~ 1489 cm^{-1} corresponds to aragonite or vaterite [84,85]. These phases were not detected in the XRD data as discussed above, but which may be present in trace amounts due to atmospheric carbonation of the samples during preparation and/or analysis here. Again the major absorption band between 1200 and 900 cm^{-1} is associated with asymmetric Si-O-T bond stretching. This particular band is the most significant in understanding the formation of reaction products [47,86]. It should be noted that for all binders formed after alkali-activation, this band shifts to lower wavenumbers and becomes narrower when compared to the unreacted precursors GGBFS and C4. Incorporation of Al tetrahedra within the gel structure is seen by a shift towards lower wavenumbers due the change in local environment and bond vibrations. In the discussion that follows, the remaining symmetrical Si-O-T bond stretching ~ 700 cm^{-1} and Si-O-T bond bending ~ 460 cm^{-1} vibration bands are considered to include contributions from substituted Al.

Increasing the curing times to 28 days resulted in narrowing of the band at ~ 950 cm^{-1}, and a shift to lower wavenumbers compared with the 2 day samples [87]. This is reported in the literature to arise from increased incorporation of Al within the silicate structure. The bands in question contain contributions from Al-O-Si linkages, of which the Al-O bonds are less stiff than Si-O [88], that result in perturbations of local Si-O bonding [89]. The C4 component is acting as an Al source, gradually increasing the number of Si-O-Al bonds within the gel structure over time.

3.2.5. Solid state nuclear magnetic resonance spectroscopy

The ^{29}Si MAS NMR spectra of the precursors (GGBFS and calcined waste clay C4) are shown in Fig. 14. The GGBFS spectrum exhibits a single broad resonance with maximum intensity at ~ – 75 ppm (Fig. 14 (a)) suggesting a wide distribution of tetrahedral Si environments Q^n(mAl) and chemical shifts. The overall chemical shift and shape indicate that low cross-linked species and/or high degrees of Al substitution dominate the GGBFS structure. This is in agreement with the glassy, highly-depolymerised nature of the precursor and with previous studies [66,90,91–93]. The GGBFS spectrum can be adequately simulated with a single peak centred at – 74.7 ppm as seen in Fig. 13 (a); it is not claimed that this is representing a single site environment, but it is a useful description of the GGBFS contribution to the spectra of hardened binders.

The complex spectrum for C4 in Fig. 14 (b) is a combination of resonances attributed to quartz, muscovite, and K-rich feldspar. The narrow resonance at – 106.6 ppm is attributed to quartz SiO_2 (Q^4) whilst the broader resonance at – 110 ppm can be attributed to a partially amorphous phase obtained as a result of clay calcination at 750 °C [7]. The

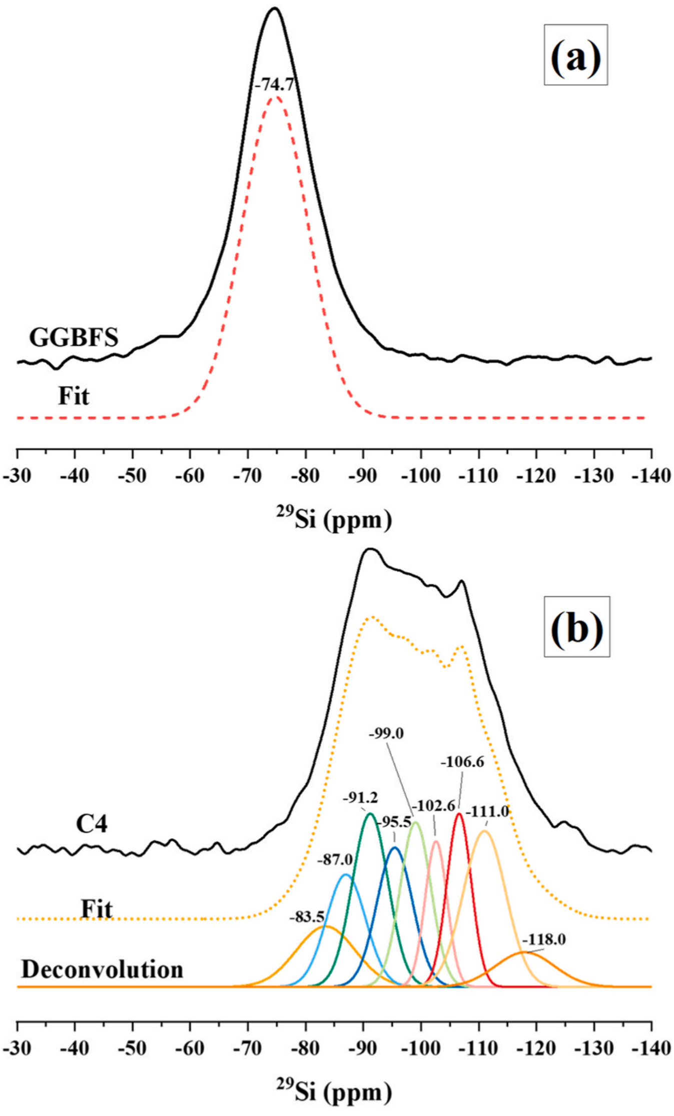

Fig. 14. ^{29}Si MAS NMR spectra of precursors: (a) GGBFS and (b) calcined C4.

main resonance bands for muscovite are found at − 87 ppm, − 91.2 ppm, and −95.5 ppm [94] along with the resonance bands of various forms of $KAlSi_3O_8$ alkali-feldspar reported in the range − 97 to − 103 ppm, assigned here as resonances at − 99 and − 102.6 ppm [94–96]. Dehydroxylation of muscovite has been reported to provide a shift of the muscovite resonances towards the feldspar region [94]. Only partial dehydroxylation of the muscovite phase may occur after calcination at 750 °C, meaning that both muscovite and the dehydroxylated phase will be present [53,97].

The deconvolution curves for the ^{29}Si MAS NMR spectra for alkali-activated GGBFS, 0C4-a, and blended 20C4-C after 2 and 28 days can be seen in Fig. 15. Five main resonance bands are identified for all spectra, centred at − 76 ppm, − 78 ppm, − 81.5 ppm, − 84 ppm, and − 89 ppm which are assigned to Q^1(I), Q^1(II), Q^2(1Al), Q^2, and Q^3(1Al) environments, respectively [91,98,99]. Q^1(I) and Q^1(II) represent two non-equivalent Q^1 environments, depending on the charge balancing ions [98]. The resonances identified are consistent with the formation of C-A-S-H type gels [100]. Table 7 gives the deconvolution results of the ^{29}Si MAS NMR spectra using Gaussian curve fitting as reported in the literature [101–103]. It is assumed that GGBFS undergoes congruent dissolution into the sodium silicate activator solution [103,104], and so its spectral contribution is described by linearly scaling the intensity of the GGBFS spectrum without adjustment to its shape or position.

The deconvolutions shown in Fig. 15 highlight a reduction in the residual GGBFS fraction in both 0C4-a and 20C4-C mixtures, along with greater C-A-S-H and reaction product formation with increased curing time from 2 to 28 days [87]. The initial degree of reaction for 0C4-a is slightly lower than that of 20C4-c at early ages, as indicated in the calorimetry data in Fig. 11(b), although 0C4-a undergoes sustained greater reaction from 2 to 28 days as shown by the larger difference in the remnant slag phase. This difference in reaction behaviour between GGBFS and the C4-GGBFS blend is expected based on the known effects of C4 inclusion. The inert quartz phase fraction acts as a filler whilst increasing the number of nucleation sites and the available interparticle space for the polycondensation reaction to proceed. The fast generation of binding phases results in high early strength, however the lack of reactivity (chemical stability) of certain mineral phases limits the degree of reaction in the following 2–28 day period [105].

Highly cross-linked Si sites such as Q^4(3Al) or Q^4(4Al) could overlap with the regions assigned to Q^3(1Al) at − 89 ppm [98,106]. It is not unreasonable to assume that the amorphous fraction identified in C4 from the comparison of its calcined and uncalcined XRD patterns (Fig. 4)

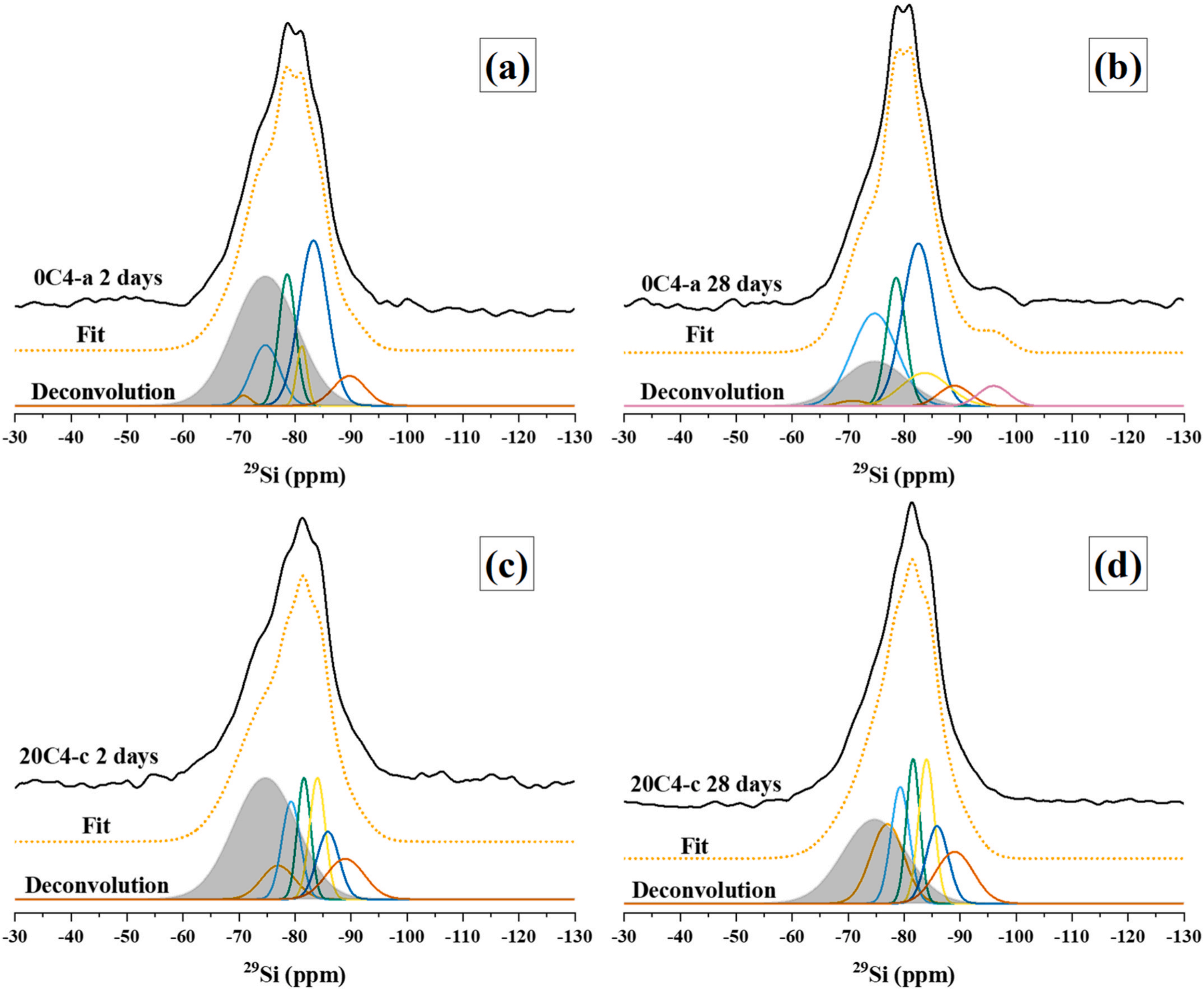

Fig. 15. ^{29}Si MAS NMR spectra with fit and deconvolution of: (a) 0C4-a 2 days, (b) 0C4-a 28 days, (c) 20C4-c 2 days, (d) 20C4-c 28 days. The grey band represents the contribution of the unreacted GGBFS which is directly scaled from the raw GGBFS spectrum under the assumption of congruent dissolution.

Table 7
Deconvolution results for ^{29}Si MAS NMR spectra of the alkali-activated blends. Estimated uncertainty in absolute site percentages is ± 2%.

Sample ID		Reaction products								Unreacted
		Q^0	Q^1 (I)	Q^1 (II)	Q^2 (1Al)	Q^2		Q^3 (1Al) or Q^4 (4Al)	Q^4 (3Al)	GGBFS
Chemical shift	ppm	-71	-76	-78	-81.5	-84	-85.5	-89	-91	-74.7
0C4-a	2 days	1%	26%	10%	3%	21%	-	4%	-	36%
	28 days	1%	23%	14%	2%	29%	9%	4%	3%	16%
20C4-c	2 days	-	8%	12%	11%	13%	11%	11%	-	34%
	28 days	-	14%	13%	13%	15%	11%	12%	-	22%

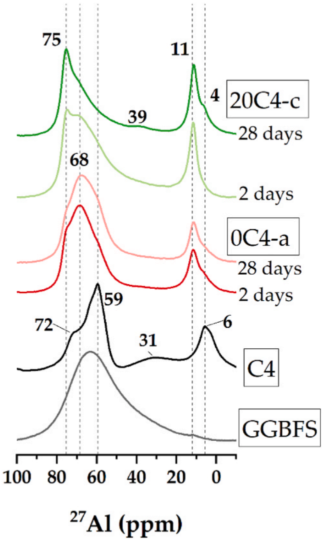

Fig. 17. ^{27}Al MAS NMR spectra for precursors GGBFS and C4, and for alkali-activated GGBFS with or without 20% calcined waste clay C4, after 2 and 28 days.

could react to form highly cross-linked N-A-S-H type gels, in addition to the C-A-S-H gel formed by reaction of the GGBFS. This process is hinted at by the increase in resonance intensity at about – 89 ppm in 20C4-c [90]. There are no significant bands corresponding to traces of the remnant waste clay C4 (Fig. 14 (b)). This is also highlighted in Fig. 16 which shows superimpositions of 0C4-a and 20C4-c at 2 days and 28 days, whereby an overall shift of the resonance towards more cross-linked species of C-A-S-H and N-A-S-H for samples containing C4 is seen.

Fig. 17 shows the ^{27}Al MAS NMR spectra of the precursors GGBFS and C4 along with the alkali-activated pastes. The broad resonance with a maximum intensity at ~ 63 ppm attributed to tetrahedral Al environments [93] is seen in the GGBFS spectrum. The broadness of the band is indicative of local disorder and asymmetry consistent with the amorphous nature of GGBFS as highlighted in the XRD data (Fig. 2) [87, 92]. Three distinct environments are identified in the ^{27}Al MAS NMR spectrum of the calcined waste clay C4. Two resonances at 72 ppm and 59 ppm within the tetrahedral Al(IV) region are associated with well defined Al tetrahedra found in alkali feldspar and muscovite. The crystal structure of muscovite consists of layers of tetrahedra (T) and octahedra (O) in a 2:1 tetrahedral to octahedral ratio (i.e. T-O-T)[107]. The resonance at ~ 6 ppm in the region below 20 ppm is associated with Al(VI) in octahedral coordination which only present in muscovite [108]. Beside the presence of Al in these well-defined coordination states, there is a weak broad signal between ~ 30–40 ppm that can be attributed to distorted tetrahedral environments of Al(V), and most likely also a broad feature underlying the sharper peaks in the Al(IV) region. The appearance of these broad bands is consistent with the amorphous content of C4 formed after calcination [109].

Fig. 17 shows the ^{27}Al MAS NMR spectra of the pastes. The resonances seen at chemical shifts of 11 ppm are attributed to the formation of hydrotalcite-group compounds which contain Al(VI) in octahedral coordination. The resonances observed in the range 80–60 ppm are associated with the formation of C-A-S-H type gels [98,101].

The narrow resonance band at ~ 75 ppm seen in the 0C4-a spectrum increases in intensity with longer curing times, representing an increase short-length ordering of C-A-S-H and greater degree of polymerisation as the reaction proceeds [70]. This resonance is associated with Al in a well-defined Al(IV) coordination and incorporated in bridging tetrahedra, whereby Al tetrahedra are bonded to Q^2(1Al) Si sites. Two main resonances are distinguishable in the 20C4-c spectrum at 75 ppm and 68 ppm. These bands also become more intense and slightly narrower with longer curing, because of increased incorporation of Al and crosslinking of the network in the form of Al(IV) bonded to Q^3(1Al) sites [91,101,110]. This may also hint at the partial formation of N-A-S-H (i.e., Q^4 sites) along with C-A-S-H, as discussed above.

3.2.6. *Mercury intrusion porosimetry*

Pore size distributions of alkali-activated materials are often classified into gel pores with diameters between 10 and 50 nm, capillary pores with diameters between 50 nm and 10 µm, and air voids above 10 µm [111]. Fig. 16displays the pore size distributions of the pastes after 28 days of curing. The predominant type of porosity seen in alkali-activated

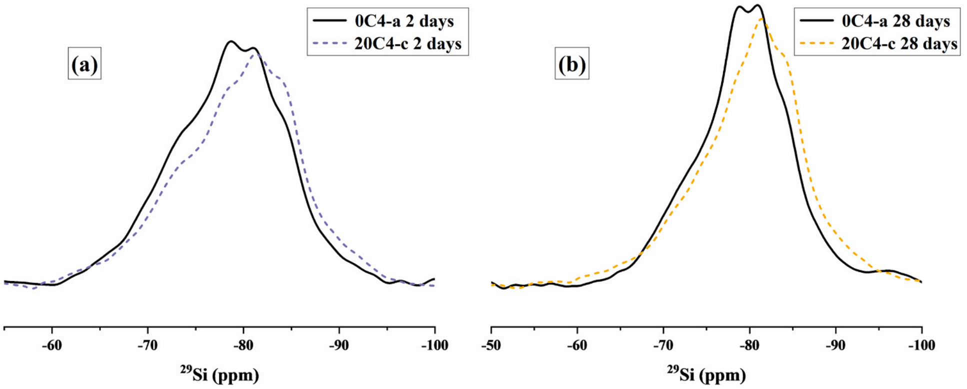

Fig. 16. ^{29}Si MAS NMR of samples 0C4-a and 20C4-c superimposed after (a) 2 days and (b) 28 days.

pastes is within the gel pore size range. 0C4-a has a well-defined peak in this region, whilst 20C4-b and 20C4-c show remarkably limited porosity in general, although may contain pores below the size range that can be accessed in these MIP experiments. No notable capillary pores are detected in any of the pastes.

Table 8 shows the measured values of total porosity for all paste samples. Samples containing C4 exhibit lower total porosity than the GGBFS-only sample. This suggests that 20C4-b and 20C4-c have formed dense binders due to effective particle dispersion with enhanced flow, and due to the higher modulus of the activating solution used. The partial formation of N-A-S-H type gel coexisting with the large amounts of C-A-S-H formed by the GGBFS may also result in a dense binder. Literature on gel coexistence has reported that this can lead to minimisation of porosity with improved material performance [15,17,112,113].

3.2.7. *Compressive strength*

The compressive strength results are shown in Fig. 17. 20C4-b samples showed similar values (43 MPa after 7 days and 61 MPa after 28 days) to the 0C4-a sample. The two mixes in question were designed to reach the same Si/Al and Na/Al molar ratios by adjusting the modulus and Na_2O dosage of the activator solution, as C4 clay has a larger Al component than GGBFS. Figs. 18 and 19.

The 20C4-c sample, with increased activator concentration with respect to the other formulations, recorded the highest 7-day strength which exceeded 60 MPa, although only a minor increase was obtained after 28 days (67 MPa). Increasing the modulus of the activator solution from 0.9 to 1.3 makes a larger concentration of soluble silica in the liquid media available for the polymerisation of both Al and Si species. This results in the formation of an enhanced gel structure, reflected in the mechanical properties especially at early ages [15].

4. Conclusions

Calcined clays from waste sources, with low metakaolin content, have been blended with GGBFS and alkali-activated using sodium silicate, and their properties were discussed.

Investigation of physical properties including particle size, morphology, and phase assemblage is necessary to understand the effect of clays in blended systems with GGBFS. It was shown that calcined waste clays have a strong effect on the fresh properties, especially on the workability of blended pastes. Clay particle size distribution and particle morphology are key factors in the mix design, requiring an understanding of their effects in blended systems.

Good workability can translate in a well-behaving binder with a dense microstructure, low porosity, and high strength. A 20 wt% calcined waste clay replacement level maintained similar compressive strength as a solely GGBFS system whilst achieving a denser binder. The quartz, muscovite and alkali-feldspar contained in the calcined clays appear to remain stable throughout the first stages of alkali-activation, whilst the reaction of the amorphous phase fraction resulted in the formation of a cross-linked binder gel.

This work has highlighted a methodology for characterising the behaviour of calcined waste clays in alkali-activation, and provides a basis for design high performance binders to accommodate clay inclusions in novel binder systems.

Table 8
Total porosities measured for alkali-activated GGBFS with and without 20 wt% calcined waste clay C4, after 2 and 28 days of curing. Error bounds represent the standard deviation among 2 replicate specimens.

Mixture	Total porosity (vol%)
0C4-a	21.07 ± 0.75
20C4-b	8.89 ± 0.69
20C4-c	5.31 ± 0.11

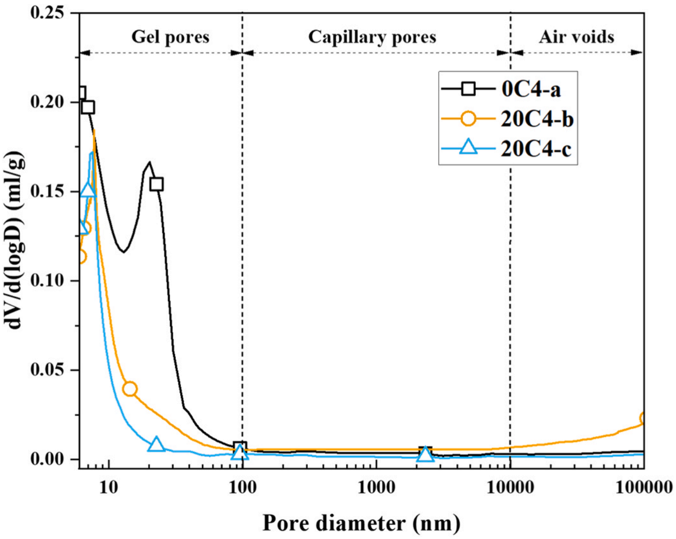

Fig. 18. Differential porosity of alkali-activated GGBFS with and without 20 wt% calcined waste clay C4, after 2 and 28 days of curing.

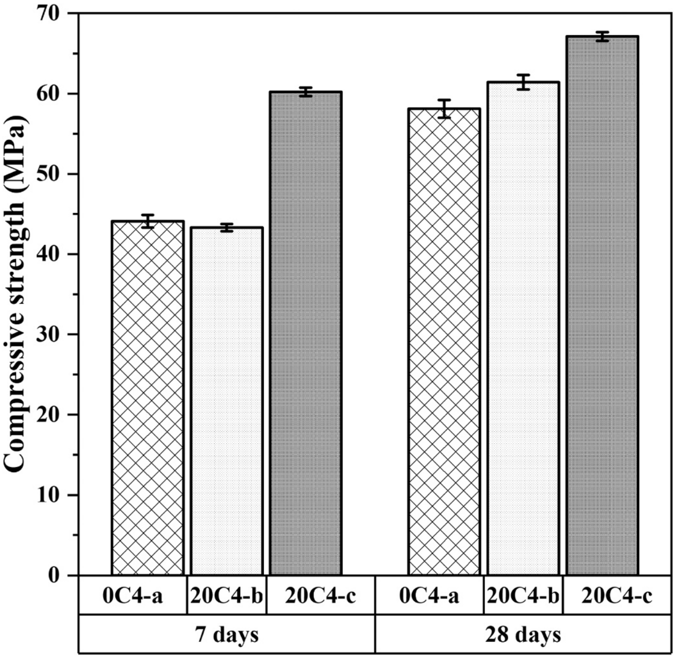

Fig. 19. Compressive strength of alkali-activated GGBFS pastes, with and without 20 wt% calcined waste clay C4.

CRediT authorship contribution statement

Brant Walkley: Supervision, Writing – review & editing. **Deeba Ansari:** Resources. **Laura Stefanini:** Conceptualization, Data curation, Investigation, Methodology, Writing – original draft. **John L. Provis:** Conceptualization, Funding acquisition, Supervision, Writing – review & editing.

Declaration of Competing Interest

The authors declare that they have no known competing financial interests or personal relationships that could have appeared to influence the work reported in this paper.

Data availability

Data will be made available on request.

Acknowledgements

This research study was carried out in the framework of the "By-products for sustainable concrete in the urban environment" (URBCON) project, funded by the Interreg North-West Europe Programme (NWE725) under the EU Cohesion Policy and financed by the European Regional Development Fund (ERDF). Furthermore, the authors wish to express their gratitude towards Ecocem for providing the GGBFS, to PQ Silicates for supplying the sodium silicate, and to Imerys for providing the clays used within this study, for the calcination and for performing the modified Chapelle test.

References

[1] A.Z. Khalifa, Ö. Cizer, Y. Pontikes, A. Heath, P. Patureau, S.A. Bernal, A.T. M. Marsh, Advances in alkali-activation of clay minerals, Cem. Concr. Res. 132 (2020), https://doi.org/10.1016/j.cemconres.2020.106050.

[2] J. Skibsted, R. Snellings, Reactivity of supplementary cementitious materials (SCMs) in cement blends, Cem. Concr. Res. 124 (2019), https://doi.org/10.1016/j.cemconres.2019.105799.

[3] F. Souayfan, E. Roziere, C. Justino, M. Paris, D. Deneele, A. Loukili, Comprehensive study on the reactivity and mechanical properties of alkali-activated metakaolin at high H_2O/Na_2O ratios, Appl. Clay Sci. 231 (2023), https://doi.org/10.1016/j.clay.2022.106758.

[4] X. Liu, J. Jiang, H. Zhang, M. Li, Y. Wu, L. Guo, W. Wang, P. Duan, W. Zhang, Z. Zhang, Thermal stability and microstructure of metakaolin-based geopolymer blended with rice husk ash, Appl. Clay Sci. 196 (2020), https://doi.org/10.1016/j.clay.2020.105769.

[5] J. Yang, L. Xu, H. Wu, J. Jin, L. Liu, Microstructure and mechanical properties of metakaolin-based geopolymer composites containing high volume of spodumene tailings, Appl. Clay Sci. 218 (2022), https://doi.org/10.1016/j.clay.2022.106412.

[6] R. Fernandez, F. Martirena, K.L. Scrivener, The origin of the pozzolanic activity of calcined clay minerals: a comparison between kaolinite, illite and montmorillonite, Cem. Concr. Res. 41 (2011) 113–122, https://doi.org/10.1016/j.cemconres.2010.09.013.

[7] S. Hollanders, R. Adriaens, J. Skibsted, Ö. Cizer, J. Elsen, Pozzolanic reactivity of pure calcined clays, Appl. Clay Sci. 132–133 (2016) 552–560, https://doi.org/10.1016/j.clay.2016.08.003.

[8] S.A. Bernal, E.D. Rodríguez, A.P. Kirchheim, J.L. Provis, Management and valorisation of wastes through use in producing alkali-activated cement materials, J. Chem. Technol. Biotechnol. 91 (2016) 2365–2388, https://doi.org/10.1002/jctb.4927.

[9] J.L. Provis, 4 - Activating solution chemistry forgeopolymers, in: J.L. Provis, J.S. J. van Deventer (Eds.), Geopolymers: Structures, Processing, Properties and Industrial Applications, 2009, pp. 50–71, https://doi.org/10.1533/9781845696382.1.50.

[10] C. Li, H. Sun, L. Li, A review: the comparison between alkali-activated slag (Si+ Ca) and metakaolin (Si+Al) cements, Cem. Concr. Res. 40 (2010) 1341–1349, https://doi.org/10.1016/j.cemconres.2010.03.020.

[11] J.L. Provis, P. Duxson, J.S.J. van Deventer, The role of particle technology in developing sustainable construction materials, Adv. Powder Technol. 21 (2010) 2–7, https://doi.org/10.1016/j.apt.2009.10.006.

[12] D.S. Perera, O. Uchida, E.R. Vance, K.S. Finnie, Influence of curing schedule on the integrity of geopolymers, J. Mater. Sci. 42 (2007) 3099–3106, https://doi.org/10.1007/s10853-006-0533-6.

[13] C. Kuenzel, L.J. Vandeperre, S. Donatello, A.R. Boccaccini, C. Cheeseman, Ambient temperature drying shrinkage and cracking in metakaolin-based geopolymers, J. Am. Ceram. Soc. 95 (2012) 3270–3277, https://doi.org/10.1111/j.1551-2916.2012.05380.x.

[14] J.J. Thomas, H.M. Jennings, Changes in the size of pores during shrinkage (or expansion) of cement paste and concrete, Cem. Concr. Res. 33 (2003) 1897–1900, https://doi.org/10.1016/S0008-8846(03)00167-4.

[15] S.A. Bernal, R. Mejía De Gutiérrez, J.L. Provis, Engineering and durability properties of concretes based on alkali-activated granulated blast furnace slag/metakaolin blends, Constr. Build. Mater. 33 (2012) 99–108, https://doi.org/10.1016/j.conbuildmat.2012.01.017.

[16] A. Buchwald, H. Hilbig, C. Kaps, Alkali-activated metakaolin-slag blends - performance and structure in dependence of their composition, J. Mater. Sci. 42 (2007) 3024–3032, https://doi.org/10.1007/s10853-006-0525-6.

[17] C.K. Yip, G.C. Lukey, J.S.J. van Deventer, The coexistence of geopolymeric gel and calcium silicate hydrate at the early stage of alkaline activation, Cem. Concr. Res. 35 (2005) 1688–1697, https://doi.org/DOI:101016/jcemconres200410042.

[18] O. Burciaga-Díaz, R.X. Magallanes-Rivera, J.I. Escalante-Garcia, Alkali-activated slag-metakaolin pastes: Strength, structural, and microstructural characterization, J. Sustain. Cem. Mater. 2 (2013) 111–127, https://doi.org/10.1080/21650373.2013.801799.

[19] S.A. Bernal, E.D. Rodríguez, R. Mejía De Gutiérrez, M. Gordillo, J.L. Provis, Mechanical and thermal characterisation of geopolymers based on silicate-activated metakaolin/slag blends, J. Mater. Sci. 46 (2011) 5477–5486, https://doi.org/10.1007/s10853-011-5490-z.

[20] X. Chen, A. Sutrisno, L.J. Struble, Effects of calcium on setting mechanism of metakaolin-based geopolymer, J. Am. Ceram. Soc. 101 (2018) 957–968, https://doi.org/10.1111/jace.15249.

[21] P. Hui, C. Chao, L. Zhen, C.C.S., L. Yang, Synthesis and reaction mechanism of an alkali-activated metakaolin-slag composite system at room temperature, J. Mater. Civ. Eng., 31, 2019. https://doi.org/10.1061/(ASCE)MT.1943-5533.0002558.

[22] J. Zhan, H. Li, Q. Pan, Z. Cheng, H. Li, B. Fu, Effect of slag on the strength and shrinkage properties of metakaolin-based geopolymers, Materials 15 (2022), https://doi.org/10.3390/ma15082944.

[23] O. Burciaga-Díaz, J.I. Escalante-García, R. Arellano-Aguilar, A. Gorokhovsky, Statistical analysis of strength development as a function of aarious parameters on activated metakaolin/slag cements, J. Am. Ceram. Soc. 93 (2010) 541–547, https://doi.org/10.1111/j.1551-2916.2009.03414.x.

[24] B. Fu, Z. Cheng, J. Han, N. Li, Understanding the role of metakaolin towards mitigating the shrinkage behavior of alkali-activated slag, Materials 14 (2021), https://doi.org/10.3390/ma14226962.

[25] A. Hasnaoui, E. Ghorbel, G. Wardeh, Optimization approach of granulated blast furnace slag and metakaolin based geopolymer mortars, Constr. Build. Mater. 198 (2019) 10–26, https://doi.org/10.1016/j.conbuildmat.2018.11.251.

[26] G.F. Huseien, J. Mirza, M. Ismail, S.K. Ghoshal, M.A.M. Ariffin, Effect of metakaolin replaced granulated blast furnace slag on fresh and early strength properties of geopolymer mortar, Ain Shams Eng. J. 9 (2018) 1557–1566, https://doi.org/10.1016/j.asej.2016.11.011.

[27] J. Zhan, H. Li, H. Li, Z. Cheng, B. Fu, Composition design and characterization of alkali-activated Slag–Metakaolin materials, Front. Built Environ. 8 (2022) 1–20, https://doi.org/10.3389/fbuil.2022.1020217.

[28] Z. Li, M. Nedeljković, B. Chen, G. Ye, Mitigating the autogenous shrinkage of alkali-activated slag by metakaolin, Cem. Concr. Res. 122 (2019) 30–41, https://doi.org/10.1016/j.cemconres.2019.04.016.

[29] L. Heller-Kallai, I. Lapides, Dehydroxylation of muscovite: study of quenched samples, Phys. Chem. Miner. 42 (2015) 835–845, https://doi.org/10.1007/s00269-015-0767-4.

[30] F. Gridi-Bennadji, B. Beneu, J.P. Laval, P. Blanchart, Structural transformations of Muscovite at high temperature by X-ray and neutron diffraction, Appl. Clay Sci. 38 (2008) 259–267, https://doi.org/10.1016/j.clay.2007.03.003.

[31] R. Deju, A. Cucos, M. Mincu, C. Tuca, Thermal characterization of kaolinitic clay, Rom. J. Phys. 66 (2021) 1–8.

[32] E. Gasparini, S.C. Tarantino, P. Ghigna, M.P. Riccardi, E.I. Cedillo-González, C. Siligardi, M. Zema, Thermal dehydroxylation of kaolinite under isothermal conditions, Appl. Clay Sci. 80-81 (2013) 417–425, https://doi.org/10.1016/j.clay.2013.07.017.

[33] E. Ferraz, S. Andrejkovičová, W. Hajjaji, A.L. Velosa, A.S. Silva, F. Rocha, Pozzolanic activity of metakaolins by the French standard of the modified Chapelle test: A direct methodology, Acta Geodyn. Geomater. 12, 2015, pp. 289–298. https://doi.org/10.13168/AGG.2015.0026.

[34] French Standard, Chapelle Test Modified, NF 18–513 Annex. A, 2012.

[35] F. Avet, R. Snellings, A. Alujas Diaz, M. Ben Haha, K. Scrivener, Development of a new rapid, relevant and reliable (R3) test method to evaluate the pozzolanic reactivity of calcined kaolinitic clays, Cem. Concr. Res. 85 (2016) 1–11, https://doi.org/10.1016/j.cemconres.2016.02.015.

[36] L. Wadsö, Operational issues in isothermal calorimetry, Cem. Concr. Res. 40 (2010) 1129–1137, https://doi.org/10.1016/j.cemconres.2010.03.017.

[37] British Standards Institution, BS EN 196–3:2016 Methods of Testing Cement - Part 3: Determination of Setting times and Soundness, 2016.

[38] Z. Tan, S.A. Bernal, J.L. Provis, Reproducible mini-slump test procedure for measuring the yield stress of cementitious pastes, Mater. Struct. 50 (2017) 1–12, https://doi.org/10.1617/s11527-017-1103-x.

[39] ASTM C109/C109M-20, Standard Test Method for Compressive Strength of Hydraulic Cement Mortars, 2020.

[40] Q. Zeng, K. Li, T. Fen-Chong, P. Dangla, Analysis of pore structure, contact angle and pore entrapment of blended cement pastes from mercury porosimetry data, Cem. Concr. Compos. 34 (2012) 1053–1060, https://doi.org/10.1016/j.cemconcomp.2012.06.005.

[41] C. Shi, R.L. Day, A calorimetric study of early hydration of alkali-slag cements, Cem. Concr. Res. 25 (1995) 1333–1346, https://doi.org/10.1016/0008-8846(95)00126-W.

[42] M.A.T.M. Broekmans, Structural properties of quartz and their potential role for ASR, Mater. Charact. 53 (2004) 129–140, https://doi.org/10.1016/j.matchar.2004.08.010.

[43] M.L. Granizo, M.T. Blanco-Varela, A. Palomo, Influence of the starting kaolin on alkali-activated materials based on metakaolin. Study of the reaction parameters by isothermal conduction calorimetry, J. Mater. Sci. 35 (2000) 6309–6315, https://doi.org/10.1023/A:1026790924882.

[44] Y. Zuo, G. Ye, Preliminary interpretation of the induction period in hydration of sodium hydroxide/silicate activated slag, Materials 13 (2020) 1–19, https://doi.org/10.3390/ma13214796.

[45] N. Li, C. Shi, Q. Wang, Z. Zhang, Z. Ou, Composition design and performance of alkali-activated cements, Mater. Struct. Constr. 50 (2017), https://doi.org/10.1617/s11527-017-1048-0.

[46] H. Peng, C. Cui, Z. Liu, C. Cai, Y. Liu, Synthesis and reaction mechanism of an alkali-activated metakaolin-slag composite system at room temperature, J. Mater. Civ. Eng. 31 (2019), https://doi.org/10.1061/(ASCE)MT.1943-5533.0002558.

[47] I. García-Lodeiro, A. Fernández-Jiménez, M.T. Blanco, A. Palomo, FTIR study of the sol–gel synthesis of cementitious gels: C–S–H and N–A–S–H, J. Sol-Gel Sci. Technol. 45 (2008) 63–72, https://doi.org/10.1007/s10971-007-1643-6.

[48] B.M. Aïssoun, S.-D. Hwang, K.H. Khayat, Influence of aggregate characteristics on workability of superworkable concrete, Mater. Struct. 49 (2016) 597–609, https://doi.org/10.1617/s11527-015-0522-9.

[49] H. Paiva, A. Velosa, P. Cachim, V.M. Ferreira, Effect of metakaolin dispersion on the fresh and hardened state properties of concrete, Cem. Concr. Res. 42 (2012) 607–612, https://doi.org/10.1016/j.cemconres.2012.01.005.

[50] C. Tournassat, I.C. Bourg, C.I. Steefel, F. Bergaya, Chapter 1 - surface properties of clay minerals, in: C. Tournassat, C.I. Steefel, I.C. Bourg, F.B.T.-D. inC.S. Bergaya (Eds.), Natural and Engineered Clay Barriers, Elsevier, 2015, pp. 5–31, https://doi.org/10.1016/B978-0-08-100027-4.00001-2.

[51] M.H. Derkani, N.J. Bartlett, G. Koma, L.A. Carter, D.A. Geddes, J.L. Provis, B. Walkley, Mechanisms of dispersion of metakaolin particles via adsorption of sodium naphthalene sulfonate formaldehyde polymer, J. Colloid Interface Sci. 628 (2022) 745–757, https://doi.org/10.1016/j.jcis.2022.07.166.

[52] M. Ben Haha, G. Le Saout, F. Winnefeld, B. Lothenbach, Influence of activator type on hydration kinetics, hydrate assemblage and microstructural development of alkali activated blast-furnace slags, Cem. Concr. Res. (2011), https://doi.org/10.1016/j.cemconres.2010.11.016.

[53] S. Guggenheim, Y.H. Chang, A.F. Koster Van Groos, Muscovite dehydroxylation: high-temperature studies, Am. Mineral. 72 (1987) 537–550.

[54] C. He, E. Makovicky, B. Osbæck, Thermal stability and pozzolanic activity of raw and calcined mixed-layer mica/smectite, Appl. Clay Sci. 17 (2000) 141–161, https://doi.org/10.1016/S0169-1317(00)00011-9.

[55] D. Constantiner, S. Diamond, Alkali release from feldspars into pore solutions, Cem. Concr. Res. 33 (2003) 549–554, https://doi.org/10.1016/S0008-8846(02)01001-3.

[56] D.M. González-García, L. Téllez-Jurado, F.J. Jiménez-Álvarez, H. Balmori-Ramírez, Structural study of geopolymers obtained from alkali-activated natural pozzolan feldspars, Ceram. Int. 43 (2017) 2606–2613, https://doi.org/10.1016/j.ceramint.2016.11.070.

[57] F. Locati, S. Marfil, E. Baldo, P. Maiza, Na_2O, K_2O, SiO_2 and Al_2O_3 release from potassic and calcic–sodic feldspars into alkaline solutions, Cem. Concr. Res. 40 (2010) 1189–1196, https://doi.org/10.1016/j.cemconres.2010.04.005.

[58] Y. Alrefaei, Y.-S. Wang, J.-G. Dai, Effect of mixing method on the performance of alkali-activated fly ash/slag pastes along with polycarboxylate admixture, Cem. Concr. Compos. 117 (2021), 103917, https://doi.org/10.1016/j.cemconcomp.2020.103917.

[59] C.K. Yip, J.S.J. van Deventer, Microanalysis of calcium silicate hydrate gel formed within a geopolymeric binder, J. Mater. Sci. 38 (2003) 3851–3860, https://doi.org/10.1023/A:1025904905176.

[60] M. Cyr, P. Lawrence, E. Ringot, Efficiency of mineral admixtures in mortars: quantification of the physical and chemical effects of fine admixtures in relation with compressive strength, Cem. Concr. Res. 36 (2006) 264–277, https://doi.org/10.1016/j.cemconres.2005.07.001.

[61] Y. Kocak, Effects of metakaolin on the hydration development of Portland–composite cement, J. Build. Eng. 31 (2020), https://doi.org/10.1016/j.jobe.2020.101419.

[62] E. Coudert, M. Paris, D. Deneele, G. Russo, A. Tarantino, Use of alkali activated high-calcium fly ash binder for kaolin clay soil stabilisation: Physicochemical evolution, Constr. Build. Mater. 201 (2019) 539–552, https://doi.org/10.1016/j.conbuildmat.2018.12.188.

[63] S.A. Bernal, R.San Nicolas, J.S.J. van Deventer, J.L. Provis, Alkali-activated slag cements produced with a blended sodium carbonate/sodium silicate activator, Adv. Cem. Res. 28 (2016) 262–273, https://doi.org/10.1680/jadcr.15.00013.

[64] A. Buchwald, R. Tatarin, D. Stephan, Reaction progress of alkaline-activated metakaolin-ground granulated blast furnace slag blends, J. Mater. Sci. 44 (2009) 5609–5617, https://doi.org/10.1007/s10853-009-3790-3.

[65] M.Ben Haha, B. Lothenbach, G. Le Saout, F. Winnefeld, Influence of slag chemistry on the hydration of alkali-activated blast-furnace slag — Part I: Effect of MgO, Cem. Concr. Res. 41 (2011) 955–963, https://doi.org/10.1016/j.cemconres.2011.05.002.

[66] S.A. Bernal, R. San Nicolas, R.J. Myers, R. Mejía De Gutiérrez, F. Puertas, J.S.J. van Deventer, J.L. Provis, MgO content of slag controls phase evolution and structural changes induced by accelerated carbonation in alkali-activated binders, Cem. Concr. Res. 57 (2014) 33–43, https://doi.org/10.1016/j.cemconres.2013.12.003.

[67] A. Machowska, Z. Kledyński, I. Wilińska, B. Pacewska, A study of the early hydration processes and properties of fly ash-slag binders, Bull. Mater. Sci. 42 (2019), https://doi.org/10.1007/s12034-019-1886-1.

[68] F. Collins, J.G. Sanjayan, Early age strength and workability of slag pastes activated by NaOH and Na_2CO_3, Cem. Concr. Res. 28 (1998) 655–664, https://doi.org/10.1016/S0008-8846(98)00025-8.

[69] E. Tajuelo Rodriguez, K. Garbev, D. Merz, L. Black, I.G. Richardson, Thermal stability of C-S-H phases and applicability of Richardson and Groves' and Richardson C-(A)-S-H(I) models to synthetic C-S-H, Cem. Concr. Res. 93 (2017) 45–56, https://doi.org/10.1016/j.cemconres.2016.12.005.

[70] B. Walkley, R. San Nicolas, M.A. Sani, S.A. Bernal, J.S.J. van Deventer, J.L. Provis, Structural evolution of synthetic alkali-activated CaO-MgO-Na_2O-Al_2O_3-SiO_2 materials is influenced by Mg content, Cem. Concr. Res. 99 (2017) 155–171, https://doi.org/10.1016/j.cemconres.2017.05.006.

[71] R.J. Myers, S.A. Bernal, J.L. Provis, Phase diagrams for alkali-activated slag binders, Cem. Concr. Res. 95 (2017) 30–38, https://doi.org/10.1016/j.cemconres.2017.02.006.

[72] S.-D. Wang, K.L. Scrivener, Hydration products of alkali activated slag cement, Cem. Concr. Res. 25 (1995) 561–571, https://doi.org/10.1016/0008-8846(95)00045-E.

[73] O. Kayali, M.S.H. Khan, M. Sharfuddin Ahmed, The role of hydrotalcite in chloride binding and corrosion protection in concretes with ground granulated blast furnace slag, Cem. Concr. Compos. 34 (2012) 936–945, https://doi.org/10.1016/j.cemconcomp.2012.04.009.

[74] J. Sun, Z. Chen, Effect of silicate modulus of water glass on the hydration of alkali-activated converter steel slag, J. Therm. Anal. Calorim. 138 (2019) 47–56, https://doi.org/10.1007/s10973-019-08146-3.

[75] K. Gao, K.-L. Lin, D. Wang, C.-L. Hwang, H.-S. Shiu, Y.-M. Chang, T.-W. Cheng, Effects SiO_2/Na_2O molar ratio on mechanical properties and the microstructure of nano-SiO_2 metakaolin-based geopolymers, Constr. Build. Mater. 53 (2014) 503–510, https://doi.org/10.1016/j.conbuildmat.2013.12.003.

[76] B.T. Poe, P.F. McMillan, C.A. Angell, R.K. Sato, Al and Si coordination in SiO_2-Al_2O_3 glasses and liquids: a study by NMR and IR spectroscopy and MD simulations, Chem. Geol. 96 (1992) 333–349, https://doi.org/10.1016/0009-2541(92)90063-B.

[77] T. Uchino, T. Sakka, M. Iwasaki, Interpretation of hydrated states of sodium silicate glasses by infrared and raman analysis, J. Am. Ceram. Soc. 74 (1991) 306–313, https://doi.org/10.1111/j.1151-2916.1991.tb06880.x.

[78] M.A. Longhi, E.D. Rodríguez, B. Walkley, Z. Zhang, A.P. Kirchheim, Metakaolin-based geopolymers: Relation between formulation, physicochemical properties and efflorescence formation, Compos. Part B Eng. 182 (2020), https://doi.org/10.1016/j.compositesb.2019.107671.

[79] Z. Zhang, H. Wang, J.L. Provis, F. Bullen, A. Reid, Y. Zhu, Quantitative kinetic and structural analysis of geopolymers. Part 1. The activation of metakaolin with sodium hydroxide, Thermochim. Acta 539 (2012) 23–33, https://doi.org/10.1016/j.tca.2012.03.021.

[80] J. Ojima, Determining of crystalline silica in respirable dust samples by infrared spectrophotometry in the presence of interferences, J. Occup. Health 45 (2003) 94–103, https://doi.org/10.1539/joh.45.94.

[81] C.Y. Heah, H. Kamarudin, A.M. Mustafa Al Bakri, M. Bnhussain, M. Luqman, I. Khairul Nizar, C.M. Ruzaidi, Y.M. Liew, Study on solids-to-liquid and alkaline activator ratios on kaolin-based geopolymers, Constr. Build. Mater. 35 (2012) 912–922, https://doi.org/10.1016/j.conbuildmat.2012.04.102.

[82] W.K.W. Lee, J.S.J. van Deventer, The effects of inorganic salt contamination on the strength and durability of geopolymers, Colloids Surf. A Physicochem. Eng. Asp. 211 (2002) 115–126, https://doi.org/10.1016/S0927-7757(02)00239-X.

[83] M.A. Trezza, A.E. Lavat, Analysis of the system $3CaO{\cdot}Al_2O_3$–$CaSO_4{\cdot}2H_2O$–$CaCO_3$–H_2O by FT-IR spectroscopy, Cem. Concr. Res. 31 (2001) 869–872, https://doi.org/10.1016/S0008-8846(01)00502-6.

[84] A.H. López, J.L.G. Calvo, J.G. Olmo, S. Petit, M.C. Alonso, Microstructural evolution of calcium aluminate cements hydration with silica fume and fly ash additions by scanning electron microscopy, and mid and near-infrared spectroscopy, J. Am. Ceram. Soc. 91 (2008) 1258–1265, https://doi.org/10.1111/j.1551-2916.2008.02283.x.

[85] A. Hidalgo, J.L. García, M.C. Alonso, L. Fernández, C. Andrade, Microstructure development in mixes of calcium aluminate cement with silica fume or fly ash, J. Therm. Anal. Calorim. 96 (2009) 335–345, https://doi.org/10.1007/s10973-007-8439-3.

[86] M. Vafaei, A. Allahverdi, Influence of calcium aluminate cement on geopolymerization of natural pozzolan, Constr. Build. Mater. 114 (2016) 290–296, https://doi.org/10.1016/j.conbuildmat.2016.03.204.

[87] B. Walkley, R.S. Nicolas, M.-A. Sani, G.J. Rees, J.V. Hanna, J.S.J. van Deventer, J. L. Provis, Phase evolution of C-(N)-A-S-H/N-A-S-H gel blends investigated via alkali-activation of synthetic calcium aluminosilicate precursors, Cem. Concr. Res. 89 (2016) 120–135.

[88] M. Król, P. Rożek, D. Chlebda, W. Mozgawa, Influence of alkali metal cations/type of activator on the structure of alkali-activated fly ash – ATR-FTIR studies, Spectrochim. Acta Part A Mol. Biomol. Spectrosc. 198 (2018) 33–37, https://doi.org/10.1016/j.saa.2018.02.067.

[89] A. Allahverdi, F. Škvára, Nitric acid attack on hardened paste of geopolymeric cements, Ceram. Silik. 45 (2001) 143–149.

[90] B. Walkley, A. Kashani, M.A. Sani, T.D. Ngo, P. Mendis, Examination of alkali-activated material nanostructure during thermal treatment, J. Mater. Sci. 53 (2018) 9486–9503, https://doi.org/10.1007/s10853-018-2270-z.

[91] S.D. Wang, K.L. Scrivener, ^{29}Si and ^{27}Al NMR study of alkali-activated slag, Cem. Concr. Res. 33 (2003) 769–774, https://doi.org/10.1016/S0008-8846(02)01044-X.

[92] S.A. Bernal, J.L. Provis, B. Walkley, R. San Nicolas, J.D. Gehman, D.G. Brice, A. R. Kilcullen, P. Duxson, J.S.J. Van Deventer, Gel nanostructure in alkali-activated binders based on slag and fly ash, and effects of accelerated carbonation, Cem. Concr. Res. 53 (2013) 127–144, https://doi.org/10.1016/j.cemconres.2013.06.007.

[93] B. Walkley, X. Ke, J.L. Provis, S.A. Bernal, Activator anion influences the nanostructure of alkali-activated slag cements, J. Phys. Chem. C 125 (2021) 20727–20739, https://doi.org/10.1021/acs.jpcc.1c07328.

[94] K.J.D. Mackenzie, I.W.M. Brown, C.M. Cardile, R.H. Meinhold, The thermal reactions of muscovite studied by high-resolution solid-state 29-Si and 27-Al NMR, J. Mater. Sci. 22 (1987) 2645–2654, https://doi.org/10.1007/BF01082158.

[95] D.H. Brouwer, 9.06 - Applications of silicon-29 NMR spectroscopy, in: : J. Reedijk, K. Poeppelmeier (Eds.), Comprehensive Inorganic Chemistry III, 3rd Edit, Elsevier, Oxford, 2023, pp. 107–137, https://doi.org/10.1016/B978-0-12-823144-9.00032-7.

[96] R. Oestrike, W. Yang, R.J. Kirkpatrick, R.L. Hervig, A. Navrotsky, B. Montez, High-resolution ^{23}Na, ^{27}Al and ^{29}Si NMR spectroscopy of framework aluminosilicate glasses, Geochim. Cosmochim. Acta 51 (1987) 2199–2209, https://doi.org/10.1016/0016-7037(87)90269-9.

[97] V. Hanykýř, J. Ederová, Z. Trávníček, J. Šrank, J. Doubek, Isothermal dehydroxylation of muscovite mica, Thermochim. Acta 93 (1985) 517–520, https://doi.org/10.1016/0040-6031(85)85130-3.

[98] R.J. Myers, S.A. Bernal, J.D. Gehman, J.S.J. van Deventer, J.L. Provis, The role of Al in cross-linking of alkali-activated slag cements, J. Am. Ceram. Soc. 98 (2015) 996–1004, https://doi.org/10.1111/jace.13360.

[99] J. Schneider, M.A. Cincotto, H. Panepucci, ^{29}Si and ^{27}Al high-resolution NMR characterization of calcium silicate hydrate phases in activated blast-furnace slag pastes, Cem. Concr. Res. 31 (2001) 993–1001, https://doi.org/10.1016/S0008-8846(01)00530-0.

[100] S.A. Bernal, J.L. Provis, V. Rose, R.Mejía De Gutiérrez, High-resolution X-ray diffraction and fluorescence microscopy characterization of alkali-activated slag-metakaolin binders, J. Am. Ceram. Soc. 96 (2013) 1951–1957, https://doi.org/10.1111/jace.12247.

[101] B. Walkley, J.L. Provis, Solid-state nuclear magnetic resonance spectroscopy of cements, Mater. Today Adv. 1 (2019), https://doi.org/10.1016/j.mtadv.2019.100007.

[102] I.G. Richardson, A.R. Brough, R. Brydson, G.W. Groves, C.M. Dobson, Location of aluminum in substituted calcium silicate hydrate (C-S-H) gels as determined by ^{29}Si and ^{27}Al NMR and EELS, J. Am. Ceram. Soc. 76 (1993) 2285–2288, https://doi.org/10.1111/j.1151-2916.1993.tb07765.x.

[103] R.J. Myers, S.A. Bernal, R. San Nicolas, J.L. Provis, Generalized structural description of calcium–sodium aluminosilicate hydrate gels: the cross-linked substituted tobermorite model, Langmuir 29 (2013) 5294–5306, https://doi.org/10.1021/la4000473.

[104] M.Ben Haha, B. Lothenbach, G. Le Saout, F. Winnefeld, Influence of slag chemistry on the hydration of alkali-activated blast-furnace slag — part II: Effect of Al2O3, Cem. Concr. Res. 42 (2012) 74–83, https://doi.org/10.1016/j.cemconres.2011.08.005.

[105] T. Oey, A. Kumar, J.W. Bullard, N. Neithalath, G. Sant, The filler effect: the influence of filler content and surface area on cementitious reaction rates, J. Am. Ceram. Soc. 96 (2013) 1978–1990, https://doi.org/10.1111/jace.12264.

[106] P. Duxson, J.L. Provis, G.C. Lukey, F. Separovic, J.S.J. van Deventer, ^{29}Si NMR study of structural ordering in aluminosilicate geopolymer gels, Langmuir 21 (2005) 3028–3036, https://doi.org/10.1021/la047336x.

[107] C. Elmi, M. Brigatti, S. Guggenheim, L. Pasquali, M. Montecchi, D. Malferrari, S. Nannarone, Sodian muscovite-2M1: crystal chemistry and surface features, Can. Mineral. 51 (2013) 5–14, https://doi.org/10.3749/canmin.51.1.5.

[108] M. Mantovani, A. Escudero, A.I. Becerro, Application of ^{29}Si and ^{27}Al MAS NMR spectroscopy to the study of the reaction mechanism of kaolinite to illite/muscovite, Clays Clay Miner. 57 (2009) 302–310, https://doi.org/10.1346/CCMN.2009.0570303.

[109] F. Souayfan, E. Rozière, M. Paris, D. Deneele, A. Loukili, C. Justino, ^{29}Si and ^{27}Al MAS NMR spectroscopic studies of activated metakaolin-slag mixtures, Constr. Build. Mater. 322 (2022), https://doi.org/10.1016/j.conbuildmat.2022.126415.

[110] K. Arbi, A. Palomo, A. Fernández-Jiménez, Alkali-activated blends of calcium aluminate cement and slag/diatomite, Ceram. Int. 39 (2013) 9237–9245, https://doi.org/10.1016/j.ceramint.2013.05.031.

[111] Y. Ma, J. Hu, G. Ye, The pore structure and permeability of alkali activated fly ash, Fuel 104 (2013) 771–780, https://doi.org/10.1016/j.fuel.2012.05.034.

[112] J.L. Provis, J.S.J. van Deventer, Alkali-Activated Materials, State-of-the-Art Report, RILEM TC 224-AAM, RILEM/, Springer, Dordrecht, 2014, https://doi.org/10.1007/978-94-007-7672-2_5.

[113] S.A. Bernal, J.L. Provis, V. Rose, R. Mejía De Gutierrez, Evolution of binder structure in sodium silicate-activated slag-metakaolin blends, Cem. Concr. Compos. 33 (2011) 46–54, https://doi.org/10.1016/j.cemconcomp.2010.09.004.